1998-06

Simulations of the proposed TJNAF 20 KW Free Electron Laser

Steele, Richard B.

Monterey, California. Naval Postgraduate School

NAVAL POSTGRADUATE SCHOOL
Monterey, California

THESIS

SIMULATIONS OF THE PROPOSED TJNAF 20 KW FREE ELECTRON LASER

by

Richard B. Steele

June 1998

Thesis Advisor: William B. Colson
Second Reader: Robert L. Armstead

Approved for public release; distribution is unlimited.

REPORT DOCUMENTATION PAGE

Form Approved
OMB No. 0704-0188

1. AGENCY USE ONLY *(Leave blank)*	2. REPORT DATE	3. REPORT TYPE AND DATES COVERED
	June 1998	Master's Thesis

4. TITLE AND SUBTITLE
SIMULATIONS OF THE PROPOSED TJNAF 20 KW FREE ELECTRON LASER

5. FUNDING NUMBERS

6. AUTHOR(S)
Steele, Richard B.

7. PERFORMING ORGANIZATION NAME(S) AND ADDRESS(ES)
Naval Postgraduate School
Monterey, CA 93943-5000

8. PERFORMING ORGANIZATION REPORT NUMBER

9. SPONSORING / MONITORING AGENCY NAME(S) AND ADDRESS(ES)

10. SPONSORING / MONITORING AGENCY REPORT NUMBER

11. SUPPLEMENTARY NOTES
The views expressed in this thesis are those of the author and do not reflect the official policy or position of the Department of Defense or the U.S. Government.

12a. DISTRIBUTION / AVAILABILITY STATEMENT
Approved for public release; distribution is unlimited.

12b. DISTRIBUTION CODE

13. ABSTRACT

As the Navy's role as peace enforcer in support of ground troops draws Navy combatants into the littoral warfare environment, surface combatants will have to deal with decreased reaction times while engaging ever-faster anti-ship missile threats. The Phalanx Close-In Weapon System (CIWS) does not offer sufficient accuracy or engagement ranges to fight these threats, and conventional chemical lasers, which operate at fixed wavelengths, lack the tunability to operate in a dynamic ocean environment.

The Free Electron Laser (FEL) offers the wavelength tunability, fast reaction times, and the pinpoint accuracy necessary to ensure protection of Navy surface combatants into the future. In support of this goal, the Navy is funding a proposed 20 kW FEL at Thomas Jefferson National Accelerator Facility (TJNAF) in Newport News, VA. This FEL will feature a klystron undulator, designed to improve gain in weak optical fields, and a loop that will feed electrons back to the accelerator. Simulations in this thesis vary the dispersive section strengths of the klystron undulator and desynchronism between the optical and electron pulses in order to find dispersive strength and desynchronism values that optimize the effects on final power and weak-field gain, while maintaining an electron energy spread less than TJNAF's goal of 6% to ensure proper feedback of electrons to the accelerator. Results show TJNAF's 20 kW FEL design will reach a final power of 19.2 kW with an energy spread of 6% at desynchronism of $d = 0.03$ using a conventional undulator.

14. SUBJECT TERMS	15. NUMBER OF PAGES
Free Electron Laser, Undulator, Klystron	71
	16. PRICE CODE

17. SECURITY CLASSIFICATION OF REPORT	18. SECURITY CLASSIFICATION OF THIS PAGE	19. SECURITY CLASSIFICATION OF ABSTRACT	20. LIMITATION OF ABSTRACT
Unclassified	Unclassified	Unclassified	UL

NSN 7540-01-280-5500

Standard Form 298 (Rev. 2-89)
Prescribed by ANSI Std. 239-18

Approved for public release; distribution is unlimited

SIMULATIONS OF THE PROPOSED TJNAF 20 KW FREE ELECTRON LASER

Richard B. Steele
Lieutenant, United States Navy
B.S., United States Naval Academy, 1990

Submitted in partial fulfillment of the
requirements for the degree of

MASTER OF SCIENCE IN APPLIED PHYSICS

from the

NAVAL POSTGRADUATE SCHOOL
June 1998

ABSTRACT

As the Navy's role as peace enforcer in support of ground troops draws Navy combatants into the littoral warfare environment, surface combatants will have to deal with decreased reaction times while engaging ever-faster anti-ship missile threats. The Phalanx Close-In Weapon System (CIWS) does not offer sufficient accuracy or engagement ranges to fight these threats, and conventional chemical lasers, which operate at fixed wavelengths, lack the tunability to operate in a dynamic ocean environment.

The Free Electron Laser (FEL) offers the wavelength tunability, fast reaction times, and the pinpoint accuracy necessary to ensure protection of Navy surface combatants into the future. In support of this goal, the Navy is funding a proposed 20 kW FEL at Thomas Jefferson National Accelerator Facility (TJNAF) in Newport News, VA. This FEL will feature a klystron undulator, designed to improve gain in weak optical fields, and a loop that will feed electrons back to the accelerator. Simulations in this thesis vary the dispersive section strengths of the klystron undulator and desynchronism between the optical and electron pulses in order to find dispersive strength and desynchronism values that optimize the effects on final power and weak-field gain, while maintaining an electron energy spread less than TJNAF's goal of 6% to ensure proper feedback of electrons to the accelerator. Results show TJNAF's 20 kW FEL design will reach a final power of 19.2 kW with an energy spread of 6% at desynchronism of $d = 0.03$ using a conventional undulator.

TABLE OF CONTENTS

ACKNOWLEDGEMENT

The author would like to gratefully acknowledge the invaluable assistance, patience, and guidance of Professor Bill Colson, Professor Bob Armstead, and Doctor Robert Wong in support of this work. The author would also like to give thanks to my wife, Mary, and daughter, Abigail for their support and encouragement.

I. INTRODUCTION

A. INADEQUATE SHIP SELF-DEFENSE

With the demise of the Soviet Union and the subsequent collapse of communism, the world's military power structure has been altered. In the past, a bipolar world with a single adversary gave the United States Navy a well-defined mission based on strong and effective strike capabilities. However, in the current world order often described as multi-polar, there is no longer a well-defined enemy based simply on national borders or ideology. In addition, the United States has been drawn into more and more small conflicts where the navy is called upon to act as a regional peace enforcer while simultaneously supporting ground forces. These peacekeeping missions close to shore often place the navy at risk from sea or land-based anti-ship missiles.

At the same time, many of the former communist countries have seen their economies take a downward turn and in a desire to strengthen the economies, many countries have sought to sell surplus weapon systems to third world countries and paramilitary groups. While many of these weapons are highly sophisticated, often the launch platforms necessary for these systems are inexpensive, small, and highly mobile. Unlike the Cold War, where overwhelming strike capabilities were considered an effective deterrent, a single anti-ship missile launched from shore or small boat can now destroy a ship and severely alter naval operations within that area. This means that with these capabilities, a third-world country with a weaker military force possesses military weapons capable of challenging United States naval forces. These weapons often utilize older technology, yet they are still able to seriously alter our military and national

strategy in areas such as the Middle East and Persian Gulf.

The Navy has responded by altering its strategy from "blue-water" or open-ocean warfare to the littoral warfare environment, where these weapons, often using less-advanced technology, have taken on increased lethality due to the shorter distances and decreased reaction times. As anti-ship missile technology increases and these missiles become faster, more maneuverable, and invisible to radar, the Navy's standard anti-ship missile defense system, the Phalanx Close-In Weapons System (CIWS) has not kept pace and fails to provide adequate ship defense. Additionally, with a 2000-meter maximum range, the CIWS is unable to engage these missiles at sufficient range to destroy them. In fact, computer simulations have shown that effective CIWS engagements occur at ranges of only 100 to 200 meters. Even if CIWS is able to engage a supersonic missile closer to maximum range, there is still a strong possibility that missile fragments would impact the ship and cause serious damage.

To counter the anti-ship missile, defensive missiles have been proposed. However, to successfully defend against anti-ship missiles, these defensive missiles will require guidance systems and maneuverability technology superior to that of anti-ship missiles. With the current mindset of downsizing and cutbacks, expensive defensive missiles may not be the answer. The United States Navy needs to consider alternatives to defend against anti-ship missile attacks.

An alternative weapon system should have a detection range that extends to the horizon, and engagement ranges must be far enough to ensure no missile debris impacts the ship. With many anti-ship missiles achieving supersonic speeds, weapon systems must have rapid reaction times and pinpoint accuracy. Decreased military budgets and an

ever-increasing number of joint operations means this weapon must also be relatively inexpensive to maintain and operate and its mission applicable across service boundaries. With anti-ship missile detection limited to the horizon at best, which means target engagement at even shorter distances, this new weapon system must deliver lethal energy to a target at the speeds in excess of the most advanced missiles to ensure the adequate defense of our ships.

B. THE FREE ELECTRON LASER (FEL)

The answer to the Navy's anti-ship missile defense may be the Free Electron Laser (FEL). While kinetic energy weapons (such as missile and projectiles) require a finite time to reach a target and, if contact is made, destroy it instantly, an FEL can deliver its energy at an impressive 186,000 miles per second, but does take a finite time to destroy a target. The high-energy laser concept has been tested with positive results using the MIRACL (Mid-Infrared Advanced Chemical Laser) at White Sands Missile Range, New Mexico. MIRACL was able to successfully engage supersonic Talos/Vandal missiles at sufficient ranges to validate the effectiveness of a high-energy laser system [1]. Based on tests at White Sands, the cost per lethal engagement was estimated to be 10 to 15 thousand dollars, which is small when compared to the cost of surface-to-air missile exercises. [2]

It has been shown that an FEL could be integrated into DDG 51 Arleigh Burke class destroyers in a space comparable to the forward gun mount [3]. In fact, the FEL weighs the same as a 32-cell VLS launcher while only occupying half the volume. The FEL would not cause an adverse effect on displacement or center of gravity, and most important, could use the available gas turbine main engines for power.

There are many environmental factors that can affect the propagation of the laser energy to the target, including atmospheric scattering, absorption, and turbulence. Scattering is caused by water molecules in the air and can be overcome by increasing the FEL power. Atmospheric absorption, on the other hand, leads to a detrimental effect known as "thermal blooming." In thermal blooming, a volume of stagnant air is heated by the powerful laser beam and acts as a negative lens that diffuses the power of the beam over a larger area. Thus, there is not sufficient power at the target to cause lethal damage. A common example of turbulence is the shimmering of a distant object on a road in the hot afternoon sun. The heat rising from the road changes the index of refraction in the air, distorting the image of that object. Since these temperature variations change the index of refraction, they can alter the propagation path of the beam and diffuse the beam energy away from the intended target.

For any shipboard laser system, a potentially harmful problem is thermal blooming. To combat thermal blooming, a crosswind must exist or an optimal wavelength, which will be less affected by atmospheric absorption, must be utilized that will ensure the greatest energy at the target. While the chances of zero wind speed are minimal while at sea, the FEL offers greater flexibility than a fixed wavelength chemical laser, as it may be designed for optimal propagation of the laser beam. This is relatively easily accomplished in an FEL by altering the magnetic field or changing the speed of the electrons. This "tunability" simply does not exist in systems such as MIRACL, which operate at a fixed wavelength.

II. THOMAS JEFFERSON NATIONAL ACCELERATOR FACILITY FEL

A. FEL USES

The Thomas Jefferson National Accelerator Facility (TJNAF) Free Electron Laser is the result of collaboration between a variety of corporate and government sponsors, most notably the United States Navy, the Department of Energy, and the state of Virginia. When online, the FEL will be used for numerous industrial and commercial applications. Some potential commercial uses include using the FEL to reduce the air drag of airplanes, making more natural-feeling nylon shirts, and using UV light to make food-packaging more resistant to bacteria. The United States Navy's goals would radically improve the defensive capabilities of U.S. Navy ships. With the moderate success of ship-defense systems such as CIWS, the FEL will fill a huge gap in ship self-defense with its speed of light arrival time and increased range. The successful development of this technology and employment onboard ship would further enhance a commanding officer's confidence in the survivability of his/her ship in the face of an anti-ship missile attack, especially as ships move into the littoral environment.

B. FEL DESIGN

The initial design of the TJNAF FEL calls for a 200-MeV electron gun that delivers a beam of electrons to a series of RF cavities called the accelerator, which will accelerate the electrons to relativistic speeds. The relativistic electron beam is magnetically focussed into an undulator of length $L = 6$ m. The undulator consists of a series of static magnetic fields alternating in the transverse direction, which cause the electron beam to bend or "wiggle" periodically. There are several ways to configure the

undulator, and the TJNAF FEL uses the klystron undulator design, which will be described in Section III. The key element of a klystron undulator consists of a dispersive section that divides the $N = 24$ undulator periods. The dispersive section allows better bunching of the electrons, and its strength is described by the dimensionless parameter, D. The klystron undulator is designed to improve gain in weak optical fields, which is useful when the weak-field gain of a conventional undulator is low for the start-up of the FEL oscillator [4]. Figure 1 is a basic FEL arrangement showing major components.

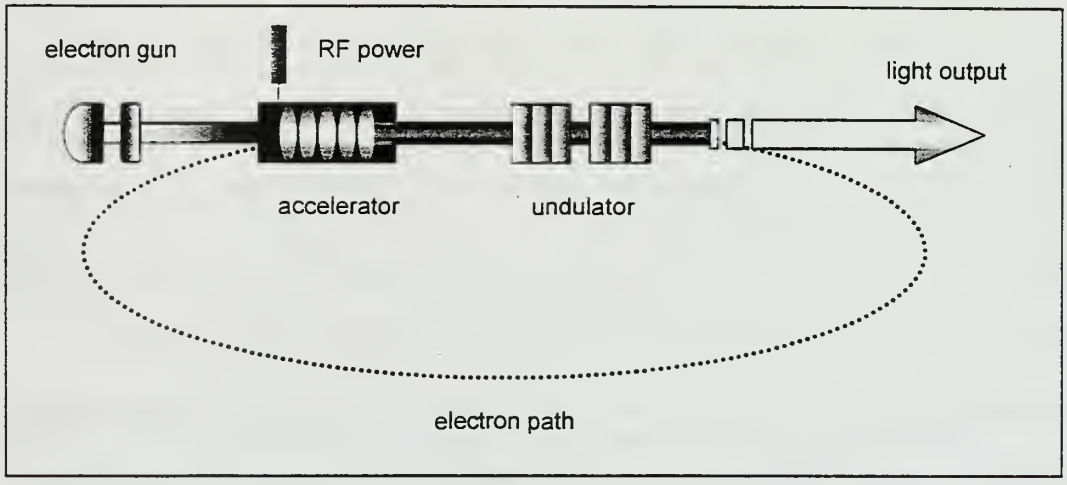

Figure 1. Basic FEL arrangement showing major components.

As the beam of electrons wiggles through the undulator, it radiates light as it is accelerated. Some of the optical power is stored between the mirrors of the resonator that allows the coupling of the electron beam to the optical wave. After many passes in the resonator, the optical power builds until the gain decreases and the optical field reaches its maximum amplitude. This is known as saturation. The energy stored in the resonator is released through a partially reflective mirror in the form of a very intense beam of 20 kW laser light. The remaining energetic electrons are fed back through the system by a

racetrack loop. These "recycled" electrons are again fed into the RF cavity of the accelerator so that they can give up the energy to the optical wave, thereby increasing the efficiency of the laser.

III. FEL THEORY

A. PHASE SPACE DIAGRAMS

The electron's interaction with the optical wave in the undulator is a key aspect of FEL design. There are typically billions of electrons travelling in a short bunch through the undulator. Macroscopically, these electrons are travelling in numerous "bunches," which all interact with the optical wave in a similar manner. Using the pendulum equation to describe the electrons and the wave equation for the optical wave, a phase space diagram is used to track the evolution of a section of the electron "bunch" one wavelength of light long through the undulator. Analysis of the phase space diagram gives much information about the performance and operation of the FEL.

Phase space is a plot of the electron's phase velocity, ν, versus the electron's phase, ζ, with respect to the optical wave. Figure 2 is a phase-space diagram with low current, $j = 2$, a moderate initial optical field, $a_0 = \pi$, and an initial phase velocity, $\nu_0 = 2.6$, which leads to maximum gain as will be explained later in this section. Each electron has an initial phase and phase velocity given by (ζ_0, ν_0) and is shown as a light gray dot. As the electrons evolve through the undulator from $\tau = 0$ at the beginning to $\tau = 1$ at the end, their movement is described by the pendulum equation (8). Their color becomes darker in Figure 2 until they appear as black dots at the end of the undulator at $\tau = 1$. Since the motion of the electrons in the undulator is described by the pendulum equation, a pendulum model will describe the interaction between the electrons and the optical field. A phase-space diagram is used to describe the electron dynamics as they traverse the length of the undulator.

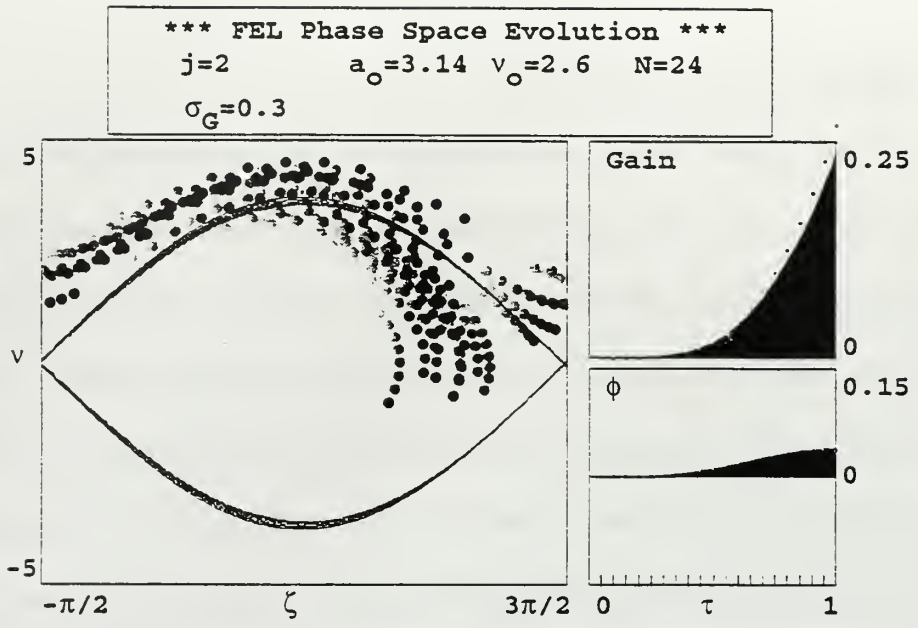

Figure 2. Phase space diagram.

In Figure 2, unstable fixed points occur at the positions $(3\pi/2,0)$ and $(-\pi/2,0)$, corresponding to a mechanical pendulum at the top of its arc. At these unstable fixed points the electron's velocity is zero and they do not evolve. A stable fixed point occurs at the position $(\pi/2,0)$, where the mechanical pendulum is at the bottom of its arc corresponding to maximum velocity. The separatrix is the curved line on the phase-space diagram going through the two unstable fixed points and separates electrons with open orbits from those with closed orbits. Electrons in open orbits correspond to a mechanical pendulum that has sufficient velocity, and thus, energy, to completely swing through the top of its arc. Electrons in closed orbits correspond to a mechanical pendulum with insufficient energy to reach the top of the arc, and thus exhibit periodic motion with less energy than the open-orbit electrons. The equation describing the separatrix is related to

the dimensionless optical field amplitude, a, and is described by:

$$\nu_S^2(\zeta_S) = 2|a|[1+\sin(\zeta_s+\phi] \tag{1}$$

The peak-to-peak height of the separatrix is $4|a|^{1/2}$, which relates the magnitude of the optical field to the size of the separatrix. As the light is amplified, the height of the separatrix also grows.

The two graphs on the right side of Figure 2 show the evolution of the gain, $G(\tau)$, and optical phase shift, $\phi(\tau)$, throughout the length of the undulator. Gain is the fractional change in energy and will be explained in a Sections E and F. As can be seen in Figure 2, initially there is no gain and no change in the optical phase. By the end of the undulator, the simulation exhibits moderate $G \approx 0.25$ with a very small optical phase shift $\phi \approx 0.03$ for the given conditions.

A monoenergetic electron beam will have all electrons with the same initial phase velocity ν_0. A maximum transfer of energy from the electrons to the light wave might be expected at resonance, $\nu = 0$. However, the electrons have a random distribution in initial phase angles, ζ_0, so that just as many electrons give up energy to the light wave as those that take energy away, which means there is no net transfer of energy and no net gain.

In order to achieve a net positive gain, the electrons are started off-resonance, so that they give up more energy to the light wave than they take away. This optimal phase velocity is $\nu_0 = 2.6$, which is the initial phase velocity chosen for Figure 2. As Figure 2 shows, the electrons begin with a random spread in phase angles, ζ, and evolve through the undulator. By the end of the undulator, the electrons have begun to bunch at $\zeta = \pi/2$, where the electrons are transferring the maximum energy to the light wave. If

$|a| >> \pi$, the electrons would have continued to evolve in phase-space, but at a less optimal phase angle, thus taking energy away from the light wave. When $|a| << \pi$, there is little electron bunching, and less transfer of energy to the light wave.

B. RESONANCE CONDITION

As electrons accelerate in the undulator of an FEL, they radiate energy in the form of light in the optical field. To achieve net gain, these electrons must transfer a net amount of energy to the optical wave. In order to transfer the optimal amount of energy, the electrons and optical field forces oscillate at resonance.

Electrons leaving the accelerator are travelling at a speed $\beta_z c$, where β_z is the axial component of velocity and c is the speed of the light wave. In Figure 3, the electron is represented by a black dot while the light wave is represented as a gray curve. As the

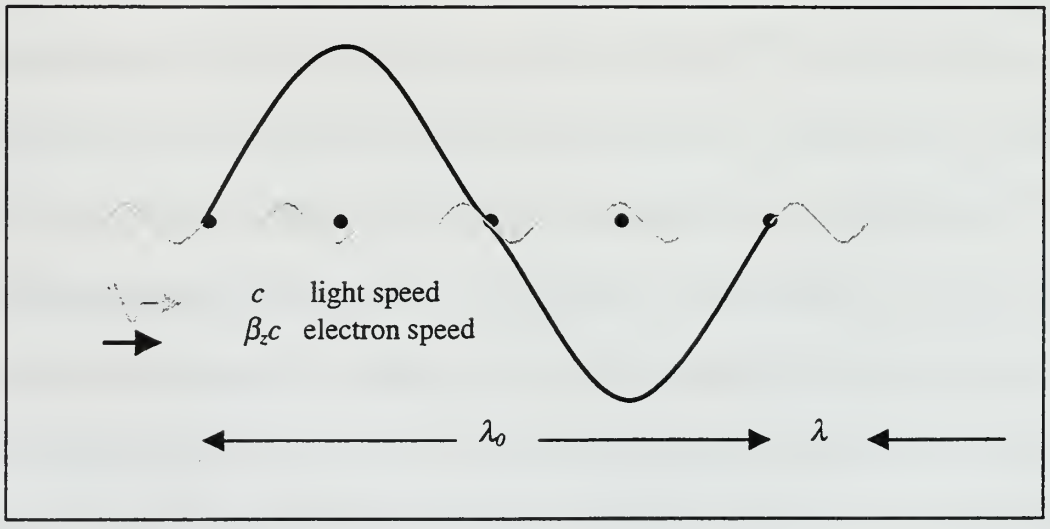

Figure 3. FEL resonance.

optical wave and electron travel from left (at $t = 0$) to right (at $t = \lambda_0 / \beta_z c$), the faster light pulse of wavelength λ passes over the electron while the electron travels one

undulator wavelength, λ_0. This is the "resonance condition" and is given by:

$$\lambda = \lambda_0 \frac{1+K^2}{2\gamma^2}, \tag{2}$$

where $K = eB\lambda_0/2\pi mc^2$ is the undulator parameter defined in Section C and γ is the relativistic Lorentz factor. This equation demonstrates one of the key advantages of FEL design over conventional lasers: wavelength tunability. By changing the electron beam energy or the magnetic properties of the undulator, the wavelength can altered without radical design changes to the FEL.

C. PENDULUM EQUATION

In order to understand the forces in the undulator, the transfer of momentum and energy between a free electron and an electromagnetic wave must be evaluated. Figure 4 is a schematic showing the x-, y-, and z-axes and electron motion through the undulator. A helical undulator field is described by $\vec{B} = B(\cos(k_0 z), \sin(k_0 z), 0)$, where $k_0 = 2\pi/\lambda_0$ is the undulator wavenumber and B is the magnetic field amplitude. The co-propagating optical magnetic field is described by $\vec{B}_s = E(\sin\psi, \cos\psi, 0)$ and the optical electric field by $\vec{E}_s = E(\cos\psi, -\sin\psi, 0)$, where B and E are the undulator magnetic and optical electric field amplitudes, respectively, and $\psi = kz - \omega t + \phi$. The optical wavenumber is $k = \omega/c = 2\pi/\lambda$ and ϕ is the optical phase. The forces acting on the electrons in the undulator are governed by the Lorentz force equations:

$$\frac{d}{dt}\left(\gamma\vec{\beta}\right) = -\frac{e}{mc}\left[\vec{E} + \vec{\beta} \times \vec{B}\right], \tag{3}$$

$$\frac{d\gamma}{dt} = -\frac{e}{mc}\vec{\beta} \cdot \vec{E}, \tag{4}$$

where e is the electron charge magnitude, m is the electron mass, c is the speed of light, $\vec{\beta} = \vec{v} / c$, and γ is called the Lorentz factor:

$$\gamma = \frac{1}{\sqrt{1 - \vec{\beta} \cdot \vec{\beta}}}. \tag{5}$$

Inserting the optical and undulator fields into (3) and integrating for relativistic electrons where $\beta_z \approx 1$ gives the velocity component in the x- and y-directions, $\vec{\beta}_\perp = (-K/\gamma)(\cos k_0 z, \sin k_0 z, 0)$, where $K = eB/k_0 mc^2$ is called the "undulator parameter." Inserting $\vec{\beta}_\perp$ into equation (4) gives

$$\dot{\gamma} = \frac{eKE}{\gamma mc} \cos(\zeta + \phi), \tag{6}$$

where the electron phase is $\zeta = (k+k_0)z - \omega t$ and $\dot{\gamma} = d\gamma / dt$.

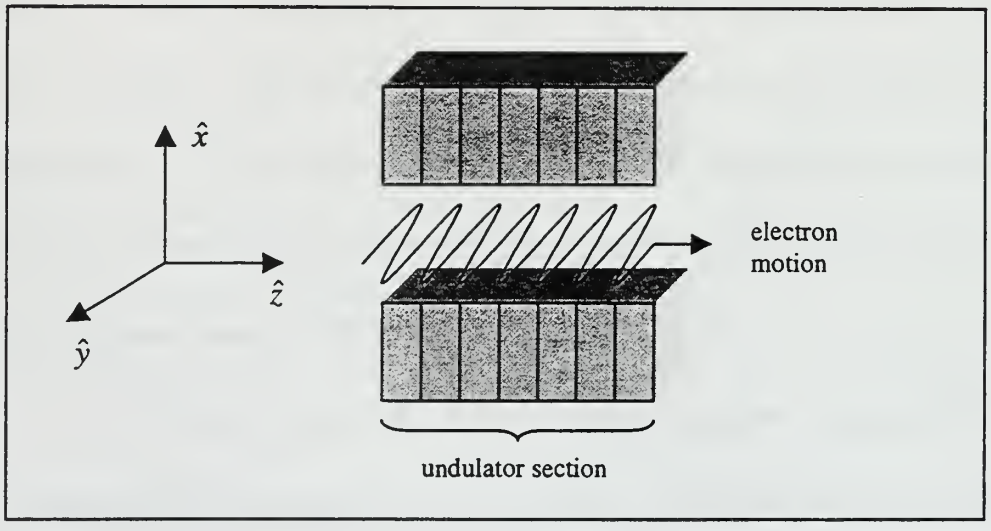

Figure 4. Diagram showing x-, y-, and z-axes in an undulator.

Substituting $\vec{\beta}_\perp$ into (5) gives a relationship between $\dot{\gamma}$ and $\dot{\beta}_z$. Using the definition of ζ, a relationship between $\dot{\gamma}$ and $\dot{\zeta}$ can be found. Using this and the

resonance condition where $\omega = \omega_0 \, 2\gamma_z^2 / (1 + K^2)$ allows (6) to be rewritten in the form

$$\ddot{\zeta} = \frac{2\omega_0 eKE}{\gamma^2 mc} \cos(\zeta + \phi) . \tag{7}$$

This is the form of the "pendulum equation" which describes the electron phase dynamics in the undulator.

Introducing the dimensionless time gives $\tau = \beta ct / L \approx ct / L$. Taking the derivative of this and inserting it into (7) gives the final form of the pendulum equation

$$\overset{oo}{\zeta} = \overset{o}{\nu} = |a| \cos(\zeta + \phi) . \tag{8}$$

where $|a| = 4\pi NeKL / \gamma^2 mc^2$ is the magnitude of the dimensionless optical field. The pendulum equation describes the motion of electrons in phase space relative to the optical wave. This motion will describe the electron's trajectory in the undulator, which can be compared to the movement of a pendulum. In phase space (ζ, ν), the electron motion will be described by open and closed orbits, which depend on the optical field amplitude, a, and the electron phase velocity, ν. Since the pendulum equation describes the electron motion in the undulator, an equation that describes the evolution of the optical wave will be derived next.

D. WAVE EQUATION

An equation describing light wave dynamics can be developed beginning with Maxwell's wave equation,

$$\left(\vec{\nabla}^2 - \frac{1}{c^2} \frac{\partial^2}{\partial t^2} \right) \vec{A}(x,t) = \frac{-4\pi}{c} \vec{J}_\perp (\vec{x}, t) \tag{9}$$

where $\vec{J}_\perp (\vec{x}, t)$ is the transverse current density. The equation describing the magnetic

field in a helical undulator is $\vec{B}_m = B_0(\cos k_0 z, \sin k_0 z, 0)$, while the electron motion is $\beta_\perp = (-K/\gamma)(\cos k_0 z, \sin k_0 z, 0)$ where $K = eB\lambda_0 / 2\pi mc^2$. The optical waveform corresponding to the magnetic polarization is $\vec{A}(\vec{x},t) = (E(\vec{x},t)/k)(\sin\psi, \cos\psi, 0)$ where $\psi = kz - \omega t + \phi(\vec{x},t)$. The electric field is $E(\vec{x},t)$ and is assumed to varying slowly in time during an optical period and slowly in *z* over an optical wavelength. This translates mathematically to mean $\dot{E} << \omega E$, $\dot{\phi} << w\phi$, $E' << kE$, and $\phi' << k\phi$, where (′) is the derivative with respect to z, while (˙) is the derivative with respect to time. These approximations allow second derivative terms to be ignored which will simplify the final form of the wave equation.

The complex electric field is defined as $\varepsilon(\vec{x},t) = E(\vec{x},t)e^{i\phi(\vec{x},t)}$, which allows the vector potential to be written as $\vec{A}(\vec{x},t) = \mathrm{Re}(\varepsilon(\vec{x},t)/k)\hat{e}e^{i(kz-\omega t)}$ where $\hat{e} = (-i,1,0)$. Now let $\alpha \equiv kz - \omega t$ so that the vector potential can be written as $\vec{A} = (\varepsilon/k)\hat{e}e^{i\alpha}$.

Inserting $\vec{A}(\vec{x},t)$ into the wave equation and using the slowly varying approximations gives

$$(\hat{e}e^{i\alpha} / k)\left(\vec{\nabla}_\perp^2 \varepsilon + 2ik\left[\pm\varepsilon' + (1/c)\dot{\varepsilon}\right]\right) = (-4\pi/c)\vec{J}_\perp,$$

where $\nabla_\perp^2 = \partial_x^2 + \partial_y^2$. Through algebraic manipulation, this can be rewritten in the form

$$\left[\frac{1}{2}\nabla_\perp^2 + ik\left(\pm\frac{\partial}{\partial z} + \frac{1}{c}\frac{\partial}{\partial t}\right)\right]\varepsilon(\vec{x},t) = -\frac{\pi k}{c}\vec{J}_\perp \cdot \hat{e}^* e^{-i\alpha}.$$

The current in the magnet is the sum over all single-particle currents, so that $\vec{J}_\perp = -ec\sum_i \beta_\perp \delta^{(3)}(x - \vec{r}_i(t))$, where $\delta(x)$ is the Dirac delta-function and $\vec{r}_i$ is the position

vector of the i^{th} electron. Using the real part of $\vec{\beta}_\perp = \Re e\left(-Ki\hat{e}e^{-ikz_0}/\gamma\right)$, results in

$$\vec{J}_\perp \cdot \hat{e}^* e^{-i\alpha} = iecK(\hat{e}^* \cdot \hat{e}) \sum_i \frac{e^{-i(k_0 z+\alpha)}}{\gamma} \delta^{(3)}(\vec{x} - \vec{r}_i(t)).$$

Define $k_0 z + \alpha = (k_0 + k)z - \omega t = \zeta$ and $\hat{e}^* \cdot \hat{e} = 2$. Since the sample electrons evolve the same way as all electrons when the volume element is much smaller than the optical pulse length, the sum term $\sum_i$ can be simplified using $\rho(\vec{x})$, the electron particle density, to weight the average over sampled electrons. Then using only the (+) solution and ζ, the wave equation becomes

$$\left[\frac{1}{2}\vec{\nabla}_\perp^2 + ik\left(\frac{\partial}{\partial z} + \frac{1}{c}\frac{\partial}{\partial t}\right)\right]\varepsilon(\vec{x},t) = -2\pi ieKk\rho(\vec{x},t)\left\langle \frac{e^{-i\zeta}}{\gamma} \right\rangle_{(\vec{x},t)},$$

where $\langle\ \rangle_{(\vec{x},t)}$ is a sample over a few electrons in a small volume element a few wavelengths of light in length at the microscopic position $(\vec{x},t)$.

Introducing dimensionless units $\tilde{z} = z - ct$ and $\tau = tc/L$, it can be found that $(\partial/\partial z + 1/c\,\partial/\partial t) = 1/L\,\partial/\partial\tau$, where the z derivatives have cancelled and L is the undulator length. The coordinate transformation allows the new coordinate site $\tilde{z}$ to follow a point in the optical field travelling at speed c. Multiply the above equation by $-4\pi iNeKL^2/\gamma_0^2 mc^2$ and define $|a| = 4\pi NeKL|\varepsilon|/\gamma_0^2 mc^2$ so that $a = |a|e^{i\phi}$ is the complex dimensionless optical field. Letting $j = 8\pi^2 Ne^2K^2L^2\rho/\gamma_0^3 mc^2$ be the dimensionless current density and assuming that the undulator is long so that $\gamma \approx \gamma_0$ for all electrons, then

$$\left(\frac{-iL}{2k}\vec{\nabla}_\perp^2 + \frac{\partial}{\partial\tau}\right)a(x,y,\tilde{z},\tau) = -\left\langle je^{-i\zeta}\right\rangle_{(x,y,\tilde{z},\tau)}. \qquad (10)$$

The first term on the left side of (10) describes diffraction. If the two terms on the left side of (10) are comparable, then diffraction is important. If the wavefront is very wide, then the first term is small when compared to the second and the diffraction term can be ignored. Also, if the electron pulse is long, then spatial dependence can be ignored which leads to the simplest form of the wave equation:

$$\overset{o}{a} = -j < e^{-i\zeta} > \tag{11}$$

where ζ is the electron phase in the pendulum equation derived earlier. As can be seen from (11), the growth of the optical field depends on the current, j. If $j = 0$, then $\overset{o}{a} = 0$, and the complex optical field does not grow. If millions of electrons are randomly distributed throughout each wavelength of light so that $< e^{-i\zeta} > \approx 0$, again the field does not grow.

E. LOW GAIN FEL

The combination of Maxwell's wave equation for the light and the relativistic Lorentz force equation for the electrons form the powerful Maxwell-Lorentz theory of the FEL that is valid in both weak and strong optical fields with high or low gain [4].

As can be seen from the wave equation, if the dimensionless current is small, $j < \pi$, then there is little change in the optical field amplitude, a, over the length of the undulator. This means $\overset{o}{a} \approx 0$, which is called the low gain limit. For weak optical fields, $|a| < \pi$, there is not much change in the electron phase velocity during the electron's evolution through the undulator. Since most FEL's operate in the low gain and weak field regime, these are good assumptions to begin the low gain derivation. In weak fields

with low current, the optical phase shift, ζ, and therefore the electron phase velocity, $v = \overset{o}{\zeta}$, can be written as a power series in a_0 using perturbation theory,

$$\zeta(\tau) = \zeta_0 + v_0\tau - \frac{a_0}{v_0^2}\left[\cos(\zeta_0 + v_0\tau) - \cos(\zeta_0) + v_0\tau\sin(\zeta_0)\right] + \ldots \tag{12}$$

$$v(\tau) = v_0 + \frac{a_0}{v_0}\left[\sin(\zeta_0 + v_0\tau) - \sin(\zeta_0)\right] + \frac{a_0^2}{v_0^3}\left[-1/4\left(\cos(2\zeta_0 + 2v_0\tau) - \cos(2\zeta_0)\right) + \cos(v_0\tau) - 1 - v_0\tau\sin(\zeta_0)\cos(\zeta_0 + v_0\tau)\right] + \ldots, \tag{13}$$

where ζ_0 is the initial electron phase, v_0 is the initial electron phase velocity, and a_0 is the initial optical field amplitude [4]. Taking the average of the electron phases, $\int_0^{2\pi}(\,)d\zeta_0 / 2\pi$, it is seen that to first order in a_0, there is no net change in energy.

Near resonance, small changes in the electron phase velocity are given by $\Delta v = 4\pi N\Delta\gamma / \gamma$ [4]. The average energy change of an electron is written as:

$$\Delta\bar{\gamma}mc^2 \approx \gamma mc^2(< v > - v_0) / 4\pi N, \tag{14}$$

The radiation energy in an elemental unit of volume dV is $2E^2dV / 8\pi$, while the number of electrons in the same unit of volume is $\rho F dV$, where $F = (r_b / w_0)^2$ and is defined as the "filling factor." Here r_b is the radius of the electron beam while w_0 is the optical field mode radius. The filling factor can be simply stated as the area of the electron beam divided by the area of the light beam.

Gain is the change in energy of the electron beam divided by the optical energy, which leads to:

$$G = -\frac{[\rho F dV][\gamma mc^2(< \nu > -\nu_0)/4\pi N]}{2E^2 dV/8\pi}. \tag{15}$$

Simplifying (15) using the average of (13) leads to the final form of the low gain equation:

$$G = j\left(\frac{2-2\cos(\nu_0\tau)-\nu_0\tau\sin(\nu_0\tau)}{\nu_0^3}\right), \tag{16}$$

where $j = 8N(e\pi KL)^2\rho F/\gamma^3 mc^2$ is the dimensionless current density defined earlier.

Figure 5 shows the final gain spectrum, G, and optical phase shift, ϕ, at the end of the undulator, $\tau = 1$, as a function of initial phase velocity, ν_0. Using TJNAF parameters with perfect beam quality, this graph shows that the peak gain occurs off-resonance at $\nu_0 = 2.6$. For low current and weak fields, the peak gain is approximated by $G = 0.135j$, which agrees well with the simulation result of $G = 0.275$ for $j = 2$.

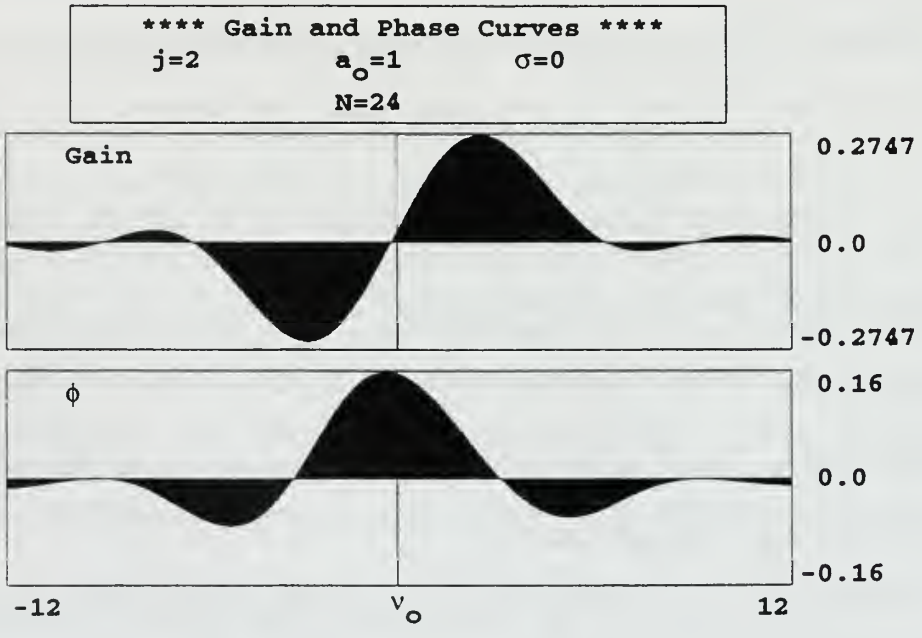

Figure 5. Weak-field gain spectrum and optical phase for low-current $j = 2$.

The gain is also anti-symmetric about ν_0, which demonstrates that a change in resonance by $\Delta\nu_0 \approx 2\pi$ can shift the gain from amplification to absorption. With this change in resonance, the electrons will take energy away from the optical wave. Figure 5 shows that the optical phase shift is symmetric about ν_0, with a peak value $\Delta\phi = 0.16$ at resonance. At the phase velocity for maximum gain, the phase shift is only $\Delta\phi = 0.04$.

F. HIGH GAIN FEL

In the high gain FEL, $j >> \pi$, the optical wave amplitude and phase change significantly during the FEL interaction, so that the assumptions used to derive the low gain equation are not valid, but the fundamental gain mechanism is still due to electron bunching in phase space [4].

Beginning with the wave equation and pendulum equation and assuming weak fields so that $|a| << \pi$, (8) is again expanded using perturbation theory and the average of the phase in terms of a, $\zeta = \zeta^{(0)} + \zeta^{(1)}$ giving $\zeta = \zeta_0 + \nu_0\tau + \zeta^{(1)}$. Substituting this form of ζ into the pendulum equation and keeping both sides of the equation in equal orders of a gives $\overset{oo(1)}{\zeta} = |a|\cos(\zeta^{(0)} + \phi)$. Substituting ζ into the wave equation and using only the first two terms of the exponential expansion gives

$$\overset{o}{a} = -j < e^{-i(\zeta_0+\nu_0\tau)} > + ij < e^{-i(\zeta_0+\nu_0\tau)}\zeta^{(1)} > . \qquad (17)$$

The first term in (17) averages to zero. For a monoenergetic beam where all electrons have phase velocity ν_0, $\overset{ooo}{a} = ij/2a(\tau)$ [4]. To solve for $a(\tau)$, we look for a solution of the form $a(\tau) = a_0 e^{\alpha\tau}$. In this case, $\alpha^3 = ij/2$. In the complex plane, $\alpha_n = (j/2)^{\frac{1}{3}} e^{i\pi(4n-3)/6}$ where n = 1, 2, 3. This means that the optical field amplitude growth is described by an

equation of the form:

$$a(\tau) = \sum_{n=1}^{3} a_n e^{\alpha_n \tau}. \tag{18}$$

To find the a_n terms, the initial conditions $a(0) = a_0$, $\overset{o}{a}(0) = 0$, and $\overset{oo}{a}(0) = 0$ are used. Putting these into the series form above and taking two derivatives and solving the three equations for three unknowns gives $a_1 = a_2 = a_3 = a_0/3$ and $\alpha_1 = (j/2)^{1/3}\left(i + \sqrt{3}/2\right)$, $\alpha_2 = (j/2)^{\frac{1}{3}}\left(i - \sqrt{3}/2\right)$ and $\alpha_3 = -i(j/2)^{1/3}$. Putting the above expressions into (18) gives

$$a(\tau) = a_0\left(e^{r\sqrt{3}\tau/2} + e^{-r\sqrt{3}\tau/2} + e^{-r\tau/2}\right)e^{ir\tau/2}/3,$$

where $r = (j/2)^{1/3}$. Using the definition of gain, $G = \frac{a^* a}{a_0^2} - 1$, results in the high gain equation:

$$G = \frac{1}{9}\left[2\cosh(r\sqrt{3}\tau) + 4\cos(r\frac{3\tau}{2})\cosh(r\frac{\sqrt{3\tau}}{2}) - 6\right]. \tag{19}$$

Note that if $j >> \pi$, $r >> 1$ so that the first term in (19) dominates and the gain at the end of the undulator, $\tau = 1$, can be approximated by

$$G \approx \frac{e^{\sqrt{3}\left(j/2\right)^{1/3}}}{9}. \tag{20}$$

Figure 6 shows the final gain spectrum at $\tau = 1$ for high-current and weak fields with perfect beam quality. The gain curve is nearly symmetric in ν_0 when compared to the low-current case of Figure 5. The peak gain is $G \approx 74$, which is orders of magnitude higher than the low-current case, but it now occurs at $\nu_0 \approx 1.6$, which is much closer to resonance. At the peak gain, the optical phase shift is $\Delta\phi \approx 1$, which is much higher than

the low-current case.

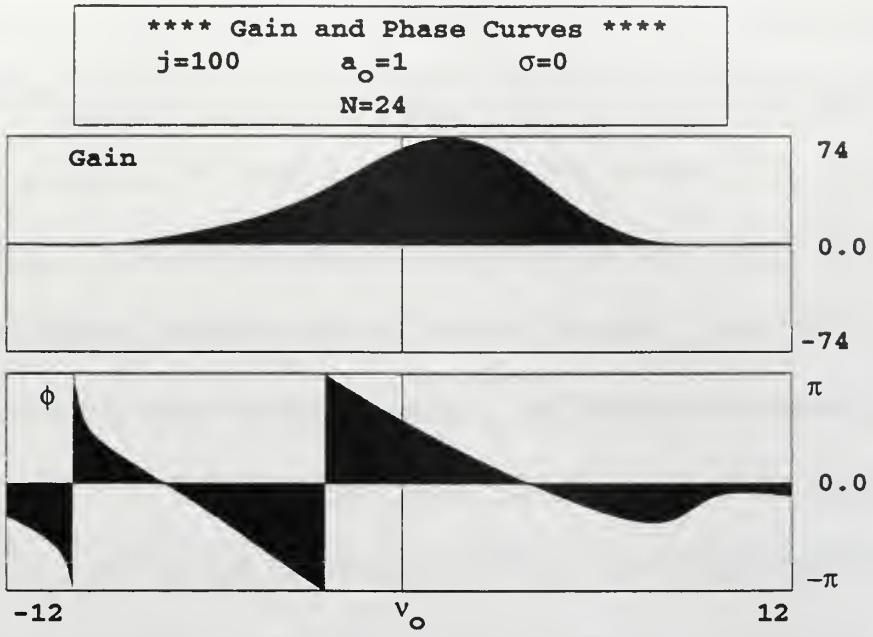

Figure 6. Weak-field gain spectrum and optical phase for high current j

G. ELECTRON BEAM QUALITY

Optimizing the FEL often leads to a design trade-off between high beam current and poor beam quality as defined by the electron beam accelerator [4]. The FEL user normally wants to maximize the dimensionless current density, $j \propto IN^3\lambda^{1/2}$. Since the number of undulator periods is fixed in the case of the Jefferson Labs FEL, $N \sim 24$, and the optical wavelength, λ, is also fixed by the application, the current density must be maximized by increasing the beam current, I. However, increasing I tends to decrease the beam quality of the accelerator. As will be shown later, TJNAF's optical klystron undulator configuration is very dependent on the quality of the electron beam.

The iterated integral form of the wave equation for weak fields is [4]:

$$\overset{o}{a}(\tau) = \frac{ij}{2}\int_0^{\tau} d\tau' \tau' F(\tau') e^{-\nu_0 \tau'} a(\tau - \tau'), \tag{21}$$

where $F(\tau) = \int dq f(q) e^{-iq\tau}$ is the Fourier transform of the distribution function of $f(q)$. If a Gaussian spread in initial electron energies is considered for a perfectly injected electron beam, the result would be a Gaussian distribution in phase velocity $f_G = \sigma_G e^{-q^2/2\sigma_G^2} / \sqrt{2\pi}\sigma_G$, where $\sigma_G = 4\pi N \overline{\Delta\gamma}/\gamma$ is the standard deviation and $\overline{\Delta\gamma}/\gamma$ is the average spread in electron energies. A random spread of width $\sigma_G \approx \pi$ causes a random phase spread $\Delta\zeta \approx \pi$ and impairs electron bunching.

A monoenergetic electron beam can also have a random spread in initial radial positions and angles. A Gaussian spread in angles, symmetric in x and y, gives the exponential distribution $f_\theta = e^{q/\sigma_\theta}$ for $q \leq 0$ and $f_\theta = 0$ for $q > 0$, where $\sigma_\theta = 4\pi N \gamma^2 \overline{\theta}^2 / (1 + K^2)$ and $\overline{\theta}$ is the rms angle with reference to the z-axis.

The characteristic function $F(\tau)$ must be found in order to evaluate the integral form of the wave equation (21). The results for the Gaussian, f_G, and exponential, f_θ, are:

$$F_G(\tau) = e^{-\sigma_G^2 \tau^2/2}, \tag{22}$$

$$F_\theta(\tau) = \frac{1}{1 - i\sigma_\theta \tau}. \tag{23}$$

If the beam quality were perfect, there would be no spread in energies or angles such that $\sigma_G = 0$ and $\sigma_\theta = 0$, and the resulting distribution functions would be delta-functions, so that $F(\tau)=1$. This means that in a perfect beam, $\overset{o}{a}$ in (21) would not be influenced

by $F(\tau')$ in determining the gain. More realistically, when the beam is not perfect, the characteristic function $|F(\tau')|$ decays within a time $\approx \sigma_G^{-1}$ or $\approx \sigma_\theta^{-1}$, reducing the effectiveness of electron feedback and decreasing the ability of the FEL to bunch electrons.

When an electron enters an undulator, even with perfect initial injection, the electron trajectories can also be altered by errors in the undulator's magnetic field. Random magnetic field errors in each undulator period will deflect electrons in the transverse direction as it enters the next period. In a typical period of the undulator, the magnetic field is described by $\vec{B} = (0, B\sin(k_0 z) + \Delta B, 0)$, where ΔB is a small undulator error. By integrating the B-field, the deflection after that period is $\Delta x \approx \sqrt{2\pi}\Delta K \lambda_0 / \gamma$, where $\Delta K = e\Delta B \lambda_0 / 2\sqrt{2}\,\pi mc^2$. This "random walk" error is not the worst problem for an FEL since the random deflections tend to cancel each other out over the length of the undulator. Engineering or design errors in undulator magnets, known as "systematic errors," can be much more harmful to FEL operation when multiplied over many undulator periods. TJNAF's klystron undulator has been engineered to such a high degree of tolerance that neither of these errors will be a problem in the performance of the 20 kW FEL.

H. SATURATION

The wave and pendulum equations are applicable in both strong and weak fields. Strong fields occur when $|a| \geq \pi$ and the electrons become trapped inside the separatrix in the closed-orbit region of phase space. As expected, the amount of electron energy converted to light is better in strong optical fields due to bunching, but gain also

decreases leading to the onset of saturation. At saturation, the FEL reaches steady-state operation, and this section will explain how it occurs.

In the resonator section, the semi-transparent output mirror allows some of the optical power to leave the resonator cavity in the form of laser light. By letting out this small amount of laser light, the optical field amplitude within the resonator is also slightly decreased. This loss, combined with other small losses within the resonator such as mirror imperfections, is characterized by the parameter Q. If the gain produced by the optical wave is greater than these resonator losses, then the optical field will grow from noise. In weak optical fields with low Q, the FEL gain may not be sufficient to overcome these losses and the steady-state power will be zero. When the optical field reaches the point where saturation begins, the gain decreases. As the gain falls-off, the optical field continues to grow but at a slower rate until the gain is insufficient to make-up for resonator losses. The growth rate of the optical field then reaches zero or steady state, where the output power of the FEL does not change. Saturation, resonator losses, and gain combine to define the steady-state output power of the FEL.

Figure 7 is a phase-space diagram with low current, $j = 2$, and strong initial optical field, $a_0 = 20$. The electrons are started off-resonance, $\nu_0 = 5$, with a random Gaussian spread of $\sigma_G = 0.3$. In the strong-field regime, the separatrix growth is proportional to the optical field strength and is described by the equation $4|a|^{1/2}$. As the height of the separatrix grows, more and more electrons are trapped in the closed orbit region of phase space. As Figure 7 shows, the electrons, initially on a downward path, have passed through the optimal phase for bunching, $\zeta + \phi \approx \pi$, and continued on to

an upward path to $\zeta + \phi \approx 0$, where they are take away energy from the optical wave. The gain is seen to rise and then decreases, marking the onset of saturation, as the

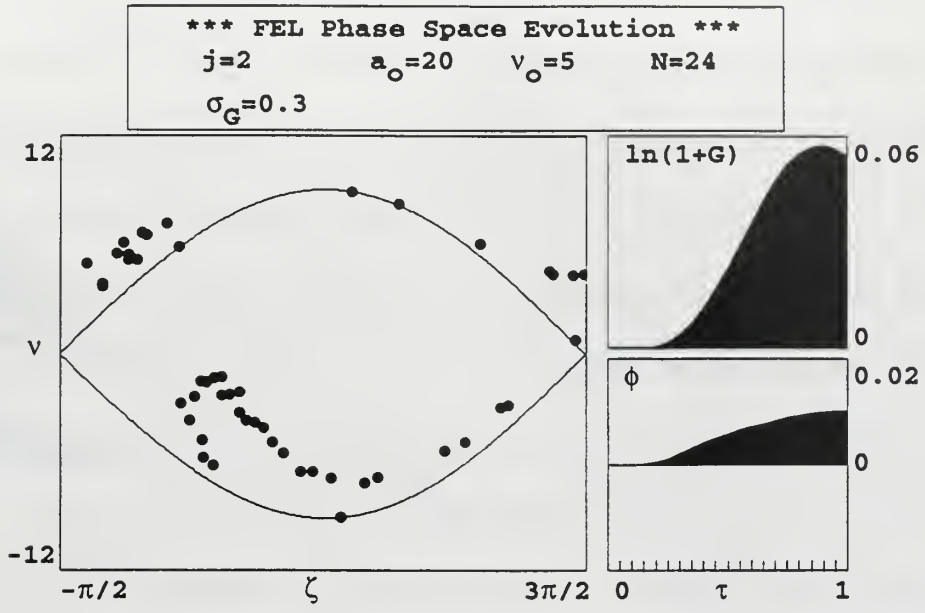

Figure 7. Strong-field phase space evolution with low current.

overbunched electrons begin to absorb energy from the light wave. The final gain, $G \approx 0.03j$ is significantly reduced from the theoretical weak-field gain, $G \approx 0.135j$.

Figure 8 shows the phase-space plot in a strong initial optical field, $a_0 = 20$, but this time with high current, $j = 100$. The initial phase velocity, $v_0 = 2$, is now closer to resonance based on information from the high-current gain curve of Figure 6. The saturation mechanism is again overbunching of the electrons caused by the strong optical field amplitude. The electrons that are near $\zeta \approx \pi$ continue on downward paths in phase space and eventually begin to overbunch. However, unlike the case of low current, as these electrons approach the bottom of their phase-space orbits, they no longer transfer energy to the optical wave, but rather they begin to drive the optical phase, ϕ. This is

indicated by a decrease in gain and a significant shift in the optical phase as shown in the lower-right plot of Figure 8.

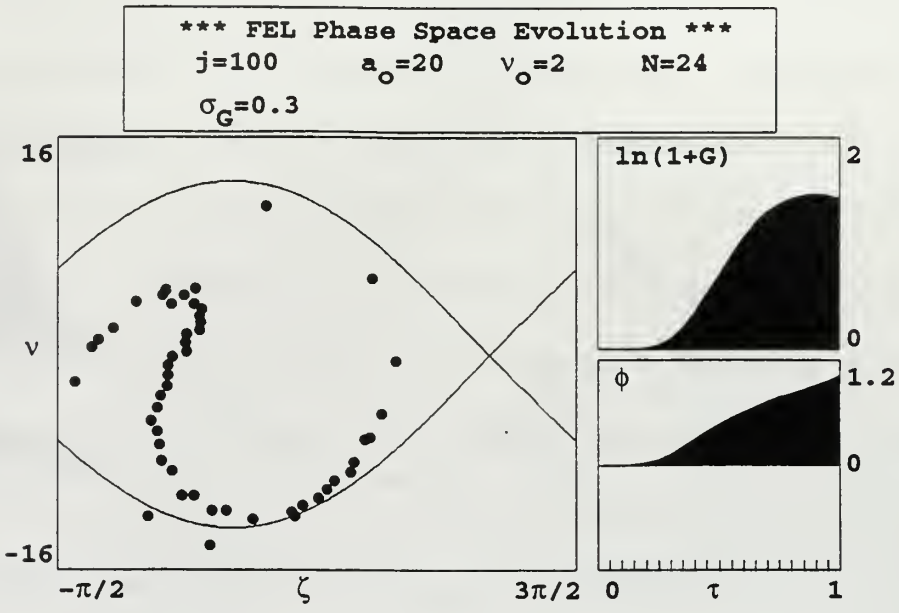

Figure 8. Strong-field phase space evolution with high current.

Although strong optical fields increase the bunching of electrons, which is one of the goals of the FEL, these strong fields eventually lead to saturation of the optical field. Figures 7 and 8 show the cases of both low and high current, where the optical field saturates due to overbunching of the electrons. In the case of high current, however, Figure 8 shows that saturation leads to a significant shift in the optical phase. Saturation is the mechanism by which the FEL achieves steady-state operation. Combining these effects of gain, resonator losses, and saturation will then be critical to successful performance of an FEL.

I. SHORT PULSE EFFECTS

Half-picosecond electron pulses will drive TJNAF's 20 kW FEL. When the length of each of these short pulses is on the order of the slippage distance, $\Delta N\lambda \approx$

1 mm, short-pulse effects will dominate electron-optical pulse coupling in the undulator. These short electron pulses entering the undulator will generate short optical pulses that bounce between resonator mirrors separated by a distance S, which is greater than the length of the undulator, L. The rebounding optical pulse arrives at the beginning of the undulator, $\tau = 0$, at time intervals of $2S/c$. The electron pulses are timed to arrive at the beginning of the undulator synchronized with the light's arrival. The term "desynchronism" is used to describe the displacement between the electron and optical pulses at the beginning of the undulator, $\tau = 0$, normalized to the slippage distance. By altering the distance between resonator mirrors, the desynchronism can be adjusted to control the arrival of the optical pulse relative to the electron pulse.

A surprising result occurs at exact desynchronism, $d = 0$, where the electron and optical pulse intervals are timed to arrive coincidentally at the beginning of the undulator. At $\tau = 0$, there is no bunching of the electrons so that there is no amplification. As the electron pulse slips back and the electrons bunch, they begin to amplify only the rear of the optical pulse, increasing the optical field amplitude. As the electrons amplify only the trailing edge of the optical pulse over several passes, the centroid of the optical pulse moves back until the electrons and optical pulse decouple, and the optical field amplitude decreases. Computer simulations for exact desynchronism have shown that as the optical pulse drifts away from the electron pulse, the optical field amplitude decreases, leaving the FEL with a steady-state power of zero. To remedy this and compensate for the distortion of the optical pulse centroid, the resonator mirrors are moved inward a small distance so that $d = -2\Delta S / N\lambda \approx 10^{-3} \rightarrow 10^{-1}$. For these cases, the optical pulse arrives at

the beginning of the undulator slightly ahead of the electron pulse. This allows a greater interaction between the optical pulse and electrons over the entire length of the undulator. As the pulses travel the length of the undulator, the electrons bunch and radiate, amplifying the trailing edge of the optical pulse. By optimizing the value of desynchronism, the optical pulse evolution will survive over many passes and steady-state power is achieved. The following figures will explore various values of desynchronism in the short-pulse effect regime.

In Figure 9, a small value of desynchronism is chosen so that $d = 0.003$. The calculation window is eight slippage distances long and travels with the light wave at speed c. The position of the short electron pulse is indicated in black at the beginning of the undulator, $\tau = 0$, and light gray at the end of the undulator, $\tau = 1$. The pulse shape is approximated as a parabola described by $j(z) = j(1 - 2z^2 / \sigma_z^2)$ for $j(z) > 0$ and zero otherwise [4]. The TJNAF pulse length is $\sigma_z = 2$ and the peak current is $j = 2$. The weak-field gain spectrum is shown in the lower middle plot. Resonator losses are determined by $1/Q$ where $Q = 20$. There is no random phase added to the electron phases so that $\delta\zeta = 0$. The evolution of the optical field is shown over n = 12,000 passes, dependent only on amplification by the electron pulse and resonator losses determined by Q.

On each pass, the unbunched electron pulse starts at $\tau = 0$ (black) and slips back to $\tau = 1$ (light gray) as bunching develops. Comparing the upper and lower left plots, as the electrons slip back along the length of the undulator, they are interacting or coupling with the optical pulse. As the electron pulse slips back, it passes through the optical field,

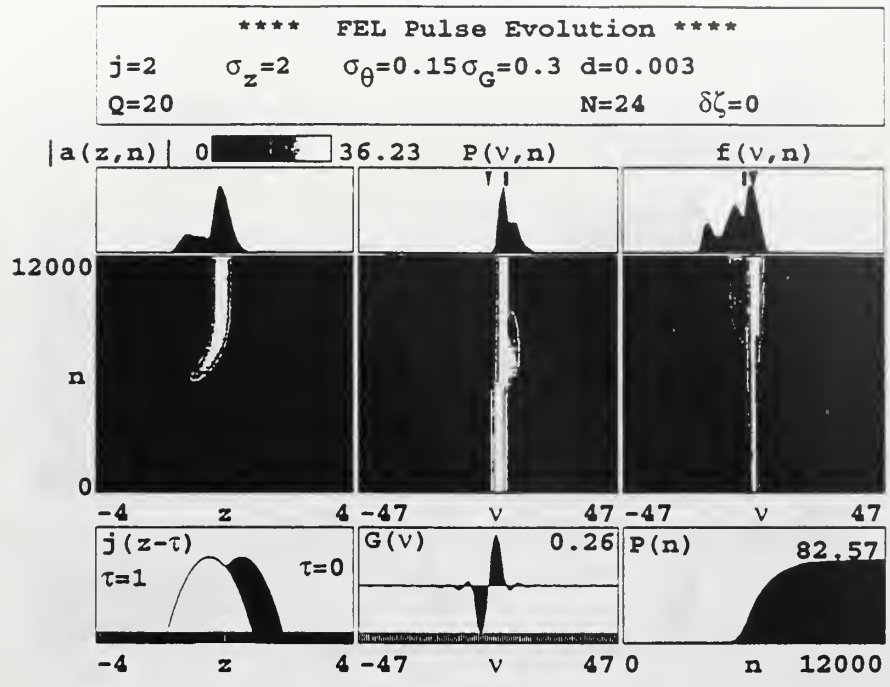

Figure 9. Short-pulse evolution at $d = 0.003$.

bunching occurs, and the optical pulse is amplified. Although this is not the maximum final power, a significant part of the electron pulse interacts with the optical field over the length of the undulator, so that the electron and light pulse couple, and a final power of $P_f \approx 82.6$ is achieved.

When d becomes too large, the electron and optical pulses do not interact over a sufficient number of passes, and the optical pulse never fully evolves, just as in the case of exact desynchronism. Figure 10 shows the pulse evolution for a larger value of $d = 0.09$. As the short electron pulse travels the length of the undulator, it interacts with the longer optical pulse. Although the electron and optical pulses interact, by the end of the undulator, the electron pulse has begun to slip behind and decouples from the trailing end of the optical pulse. Thus, the final power is reduced reaching a steady-state value of $P_f \approx 20.9$.

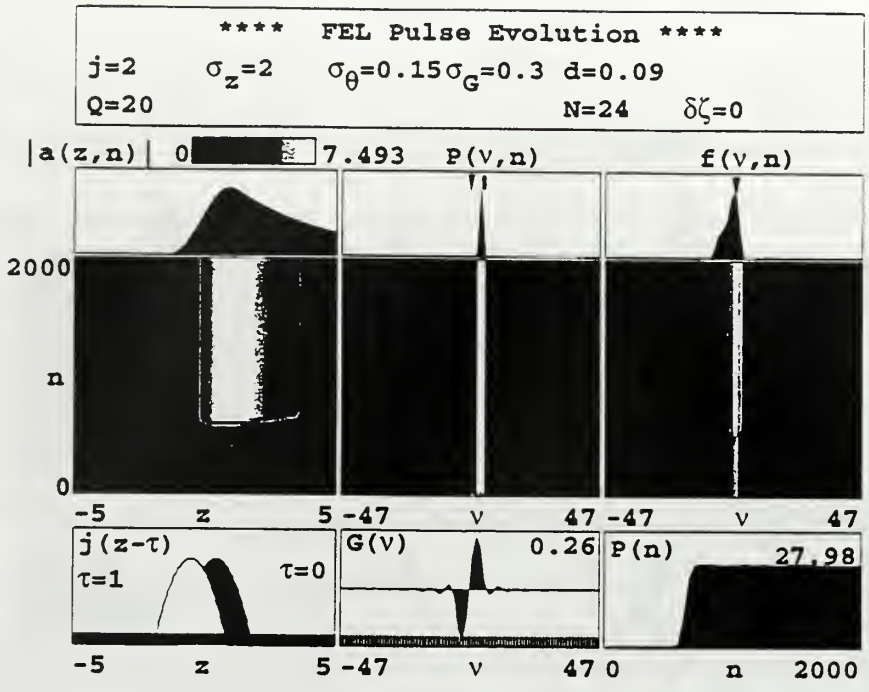

Figure 10. Short-pulse evolution for $d = 0.09$.

These two examples have shown the importance of desynchronism on steady-state power and optical pulse shape. The importance of desynchronism to pulse evolution and saturation, where short-pulse gain is greater than resonator losses, will be shown in further computer simulations with varying d in Chapter IV.

J. OPTICAL KLYSTRON UNDULATOR

In this section, a specific undulator design, the klystron undulator, will be explored. The main benefit of the klystron undulator is to increase gain in weak optical fields. This increased gain comes at the expense of power at saturation, and, as will be shown later, the optical klystron undulator is sensitive to electron beam quality.

The standard design of the optical klystron is shown in Figure 11. It consists of two sets of undulator magnets called the "modulator" and the "radiator." Separating the undulator magnets is a dispersive section or drift space. The purpose of the first set of

undulator magnets, or the modulator section, is to prepare the electrons for bunching as they travel through the dispersive section or drift space. As the electrons enter the

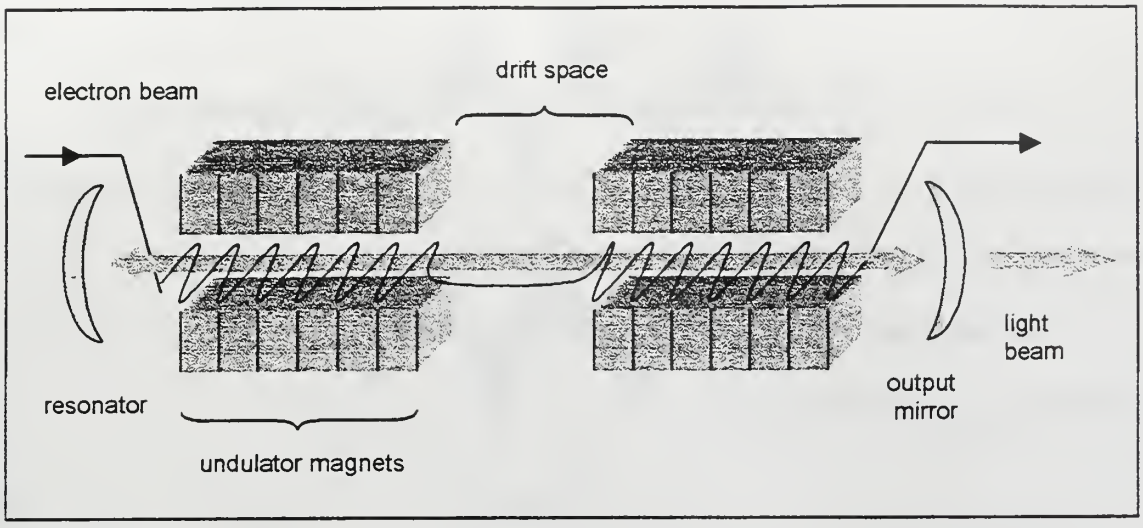

Figure 11. Optical klystron undulator with drift space.

dispersive section, the coupling between the optical field and electrons stops because there is no undulator field. In a dispersive section, a strong magnetic field is produced by bending magnets placed between the undulator sections. The result is that the electrons can be bunched in weak fields as they enter the radiator section of undulator magnets. The bunched electrons are now able to transfer more energy to the optical wave as they pass through the radiator section of undulator magnets.

As the optical wave and electrons interact throughout the two undulator sections, the wave and pendulum equations describe their evolution, so that:

$$\overset{oo}{\zeta} = \overset{o}{\nu} = |a|\cos(\zeta + \phi), \tag{8}$$

$$\overset{o}{a} = -j < e^{-i\zeta} >, \tag{11}$$

for $0 \leq \tau \leq 0.5$ and $0.5 < \tau \leq 1$. Between the two sets of undulator magnets, the equations

in the drift space or dispersive section are

$$\Delta\zeta = \nu D, \tag{24}$$

$$\Delta\nu = 0 \tag{25}$$

at $\tau = 0.5$, where D is the dimensionless parameter describing the strength of the dispersive section or the length of the drift space. These equations are valid in both weak and strong optical fields with high or low currents [4].

In weak fields with low gain, the wave and pendulum equations can be solved analytically to give the final gain at $\tau = 1$, [4],

$$G(\nu_0) \approx \frac{jD}{4}\sin(\nu_0 D). \tag{26}$$

This gain equation assumes that $D \to \infty$ and $\nu_0 \to 0$ with the product $D\nu_0$ fixed. Figure 12 shows the gain spectrum for a klystron with a dispersive strength of $D = 1$ in weak fields with low current. It assumes a perfect electron beam. The numerous peaks at $|\nu_0| < 2\pi$ occur because of the interference between the two sets of undulators, and the peak gain has risen to $G \approx 0.82$. This is three times the gain of the conventional undulator, which had a gain $G = 0.27$ for the same value of j.

As equation (26) shows, the peak gain for a klystron undulator is $jD/4$ at a phase velocity $\nu_0 = \pi/D$. Also, the beam quality should be good enough to ensure that the initial phase velocity spread is $\Delta\nu_0 \leq \pi/D$. As the strength of the dispersive section, D, increases, the initial spread in phase velocities must be even narrower, which requires a higher quality electron beam than a conventional undulator, where the initial phase velocity spread is only $\Delta\nu_0 \leq \pi$.

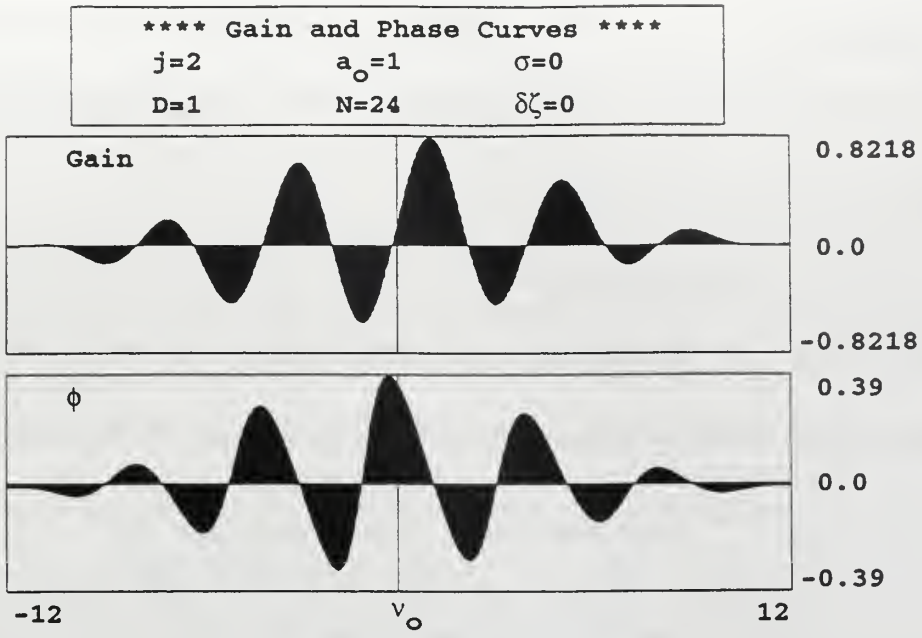

Figure 12. Gain spectrum for a low-current, weak-field optical klystron FEL.

K. TRAPPED-PARTICLE INSTABILITY

In strong optical fields, the height of the separatrix is large and the electrons become trapped in closed orbits in phase space. The amount of energy converted to light, or the efficiency, is greater, but while in these closed orbits, the electrons can become trapped in deep potential wells in phase space. These trapped electrons will oscillate at the synchrotron frequency which can then drive the carrier wave unstable causing the development of sidebands from noise. Although a narrow power spectrum with no sidebands is often the goal, sidebands allow the FEL to achieve higher powers, which may interfere with certain applications.

As the FEL reaches saturation, the trapped electrons begin to oscillate at the trapped-particle or synchrotron frequency given by $\nu_s \approx |a|^{1/2}$. Sidebands appear around the fundamental phase velocity at $\nu_0 \pm \nu_s$, and are shifted from the fundamental

wavelength by $\Delta\lambda / \lambda = \nu_s / 2\pi N$. An optical field amplitude of $|a| \approx 4\pi^2 \approx 40$ causes one synchrotron oscillation as τ goes from 0 to 1, which corresponds to a peak-to-peak separatrix height of $4|a|^{1/2} \approx 25$.

Figure 13 shows a phase-space plot for low current, $j = 2$, and strong initial optical field, $a_0 = 40$. Electrons are started off-resonance with a phase velocity of $\nu_0 = 2$ with a Gaussian spread in velocities of $\sigma_G = 0.3$. In this case, the initial optical field is

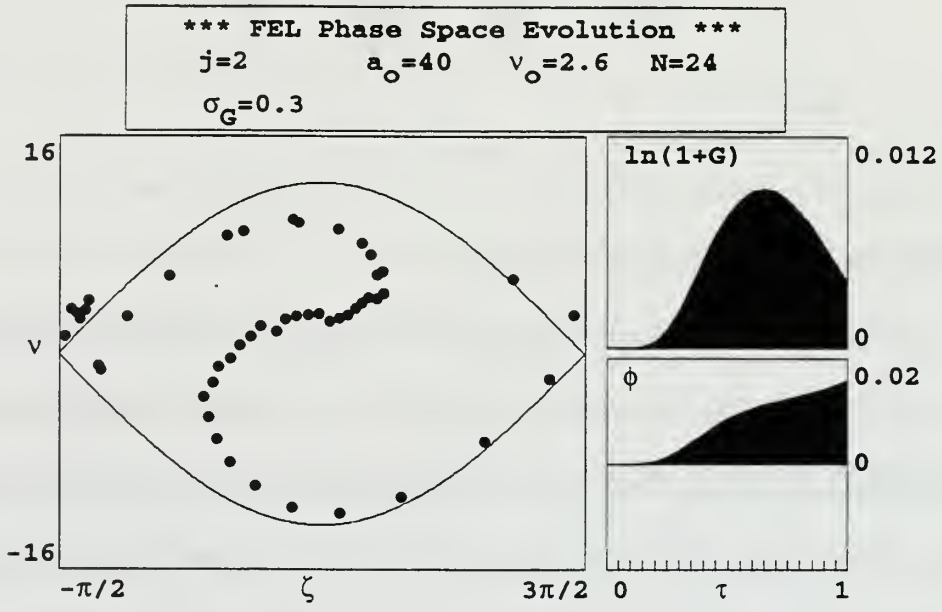

Figure 13. Phase space evolution demonstrating trapped-particle instability.

sufficient for trapped-particle instability and a full synchrotron oscillation of the electrons. As the electrons bunch in strong optical fields, the electrons pass through the optimal phase for bunching, $\zeta + \phi \approx \pi$, and overbunch as they are trapped in the potential wells due to the strong optical field. This overbunching causes saturation and a decrease in the final gain.

The trapped-particle instability and the subsequent growth of sidebands can lead

to both desired and undesired effects in FEL performance. For some FEL experiments, a narrow power spectrum with no sidebands is a desired feature. Depending on the desired result, designers can also modify resonator losses (determined by Q) or the electron beam current (characterized by j), to influence the onset of the trapped-particle instability. This, however, can also lead to degraded FEL performance, which is a trade-off designers must take into account.

IV. SIMULATION RESULTS

A. FINAL POWER

Figure 14 shows the output from a simulation of Thomas Jefferson National Accelerator Facility (TJNAF) 20 kW FEL. The dimensionless current density is $j = 2$, the electron pulse length is $\sigma_z = 2$, resonator losses are determined by $Q = 20$, and for this case the desynchronism is $d = 0.007$. In the undulator, there are $N = 24$ periods for the conventional undulator, $D = 0$. The electron beam has a Gaussian spread in angles and phase velocities with a standard deviation $\sigma_\theta = 0.15$ and $\sigma_G = 0.3$, respectively, with no random phase displacement so that $\delta\zeta = 0$. The number of passes in the resonator is $n = 2000$.

The electron pulse, approximated with a parabolic shape, is illustrated in the lower-left plot at the beginning $(\tau = 0)$ in black and end $(\tau = 1)$ of the undulator in gray. In the upper-left plot, the optical field amplitude $|a(z,n)|$ at each pass n in the resonator is plotted. The scale ranges from zero in black to the maximum value shown as white. The final optical field amplitude is shown above the optical field evolution. The bottom-center graph shows the weak-field gain spectrum as a function of phase velocity $G(v)$. Above this is a plot of the power spectrum as a function of phase velocity at each pass n in the resonator $P(v,n)$. The total power evolution $P(n)$ at each pass n is shown in the lower right plot. The upper-right plot represents the spread in electron energy at each pass n in the resonator. The width of this line, Δv, can be found using the relation $\Delta v = 4\pi N \Delta\gamma / \gamma$, where γ is the relativistic Lorentz factor.

The small desynchronism in Figure 14 has caused the electron pulse to amplify the leading edge of the optical pulse at the beginning of the undulator as it slips to the trailing edge by the end of the undulator. Since the electron pulse is depositing gain over the entire optical pulse on each pass, the peak optical field strength reaches $|a| = 25$. As

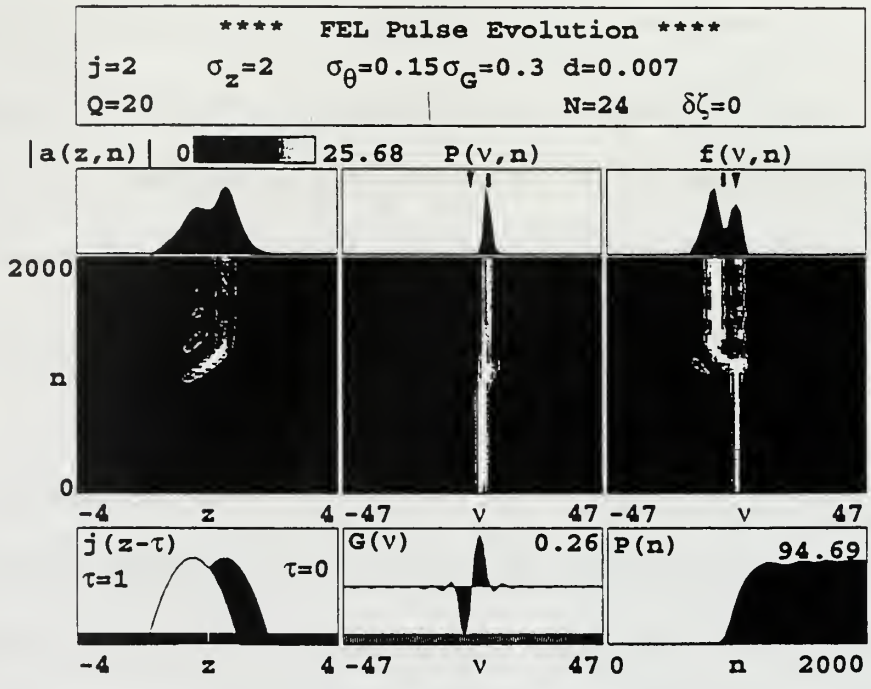

Figure 14. Pulse evolution for $D = 0$ at $d = 0.007$.

the electron pulse amplifies the optical pulse, it continually modulates the optical wave. This modulation can be clearly seen after $n \approx 900$ passes where the optical field amplitude reaches its peak value. The trapped-particle instability begins to distort the optical pulse in strong fields, but the optical field weakens so that the pulse reaches steady state after $n \approx 1700$ passes. The power spectrum shows that a small sideband developed as the trapped-particle instability occurred, but then disappeared as the optical field amplitude decreased. After reaching steady state, the smooth optical pulse leads to a narrow power spectral linewidth as shown in the upper-center plot. The bottom-center

plot, $G(\nu)$, shows the weak-field gain discussed in Section E. In the upper-right plot, the evolution of the electron's phase velocity distribution increases in spread as the stronger optical field extracts more energy from the optical pulse. The two peaks in the energy spectrum plot $f(\nu,n)$ are the original electron energy (right peak) and the energy of electrons trapped in strong fields (left peak). The lower-right plot shows that optical power grows to saturation at $n \approx 1000$ passes and reaches a final value of $P_f = 94$. The trapped-particle instability has imposed a periodic modulation on the optical pulse shape.

Figure 15 uses the same beam parameters, but with a larger desynchronism $d = 0.05$. The larger desynchronism has advanced the optical pulse ahead of the electron pulse, so that the shorter electron pulse is now amplifying only the trailing edge of a much longer optical pulse on each pass. This leads to a decoupling of the optical pulse and electrons, so that the peak optical field amplitude is $|a| = 13$. This optical field

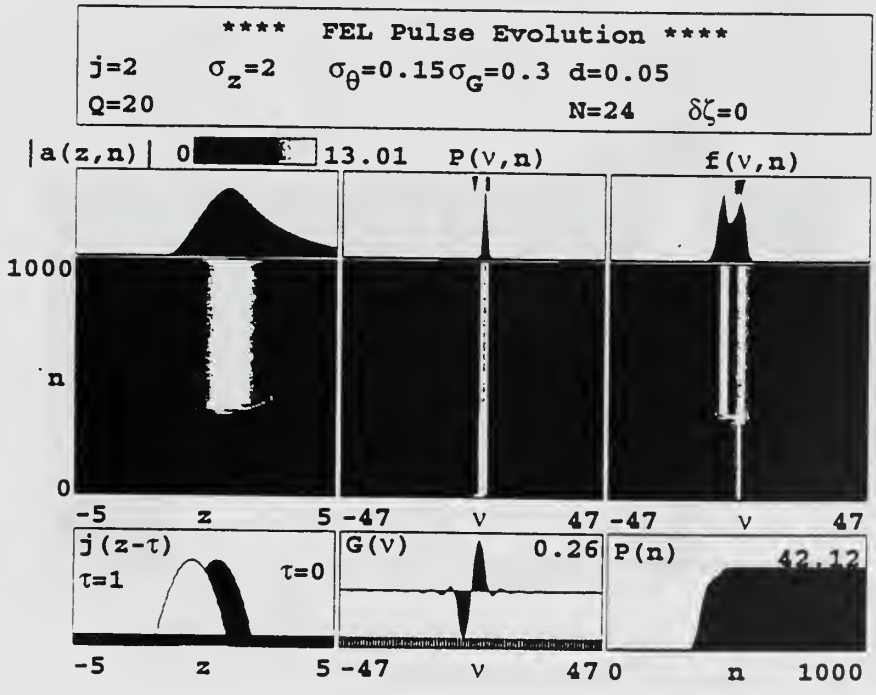

Figure 15. Pulse evolution for $D = 0$ at $d = 0.05$.

strength is not sufficient for the trapped-particle instability and the optical pulse saturates at $n \approx 300$, where the optical pulse develops a smooth exponential shape. As shown in the power spectrum plot $P(\nu,n)$, there are no sidebands, and the smooth optical pulse leads to a narrow linewidth. The spread in electron energies is shown in the $f(\nu,n)$ plot in the upper right. The final power is now only $P_f = 42$ because the electrons start near the trailing edge of the optical pulse, and drop back out of the optical field before the end of the undulator.

Figure 16 shows the FEL pulse evolution for an even larger value of desynchronism $d = 0.11$. Steady state is achieved after $n \approx 2500$ passes, and the optical power, $P(n)$, and optical pulse shape, $|a(z,n)|$, do not appear to evolve any further. The final power, $P_f = 9$ is significantly reduced by a factor of 10 when compared to the

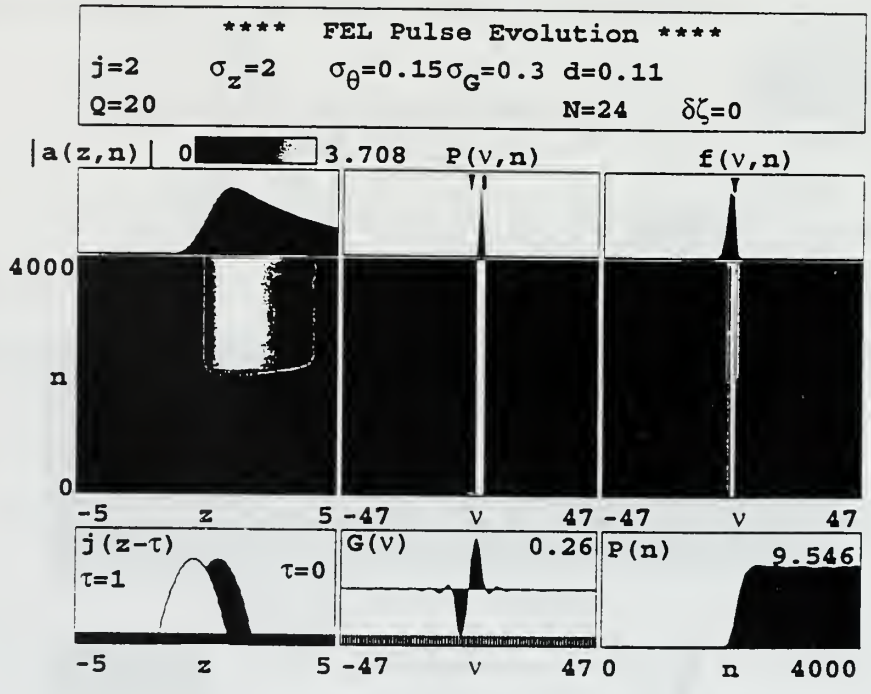

Figure 16. Pulse evolution for $D = 0$ at $d = 0.11$.

smaller desynchronism case of Figure 14. The peak optical field amplitude is now $|a| = 3.7$, and is not sufficient for the trapped-particle instability. On each pass, the short electron pulse is only amplifying the trailing edge of a much longer optical pulse, while the large desynchronism is artificially advancing the front edge of the optical pulse well ahead of the electrons. Much of the optical pulse is ahead of the electron pulse, and is decoupled from electrons. The long pulse is coherent and has a narrow power spectrum, $P(\nu,n)$. There are no sidebands in the weak optical fields, and the resulting electron spectrum, $f(\nu,n)$ is narrow.

For Figures 17-19, the klystron undulator has a dispersive strength of $D = 1$. All other electron beam and resonator parameters remained the same.

Figure 17 shows the pulse evolution for small desynchronism $d = 0.003$. The optical field reaches single-mode saturation at $n \approx 750$ passes. The power increases, and

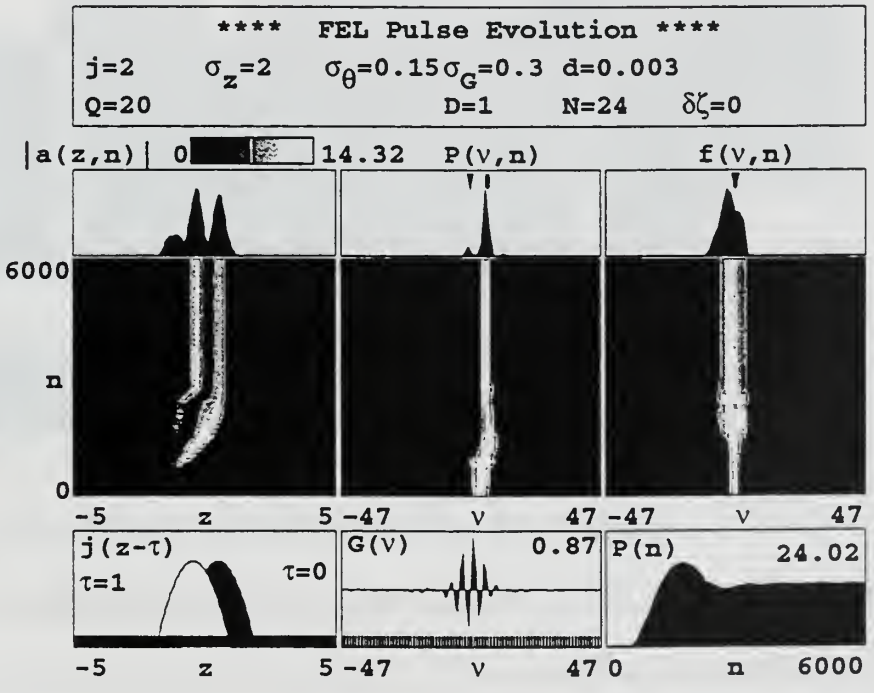

Figure 17. Pulse evolution for $D = 1$ at $d = 0.003$.

reaches a final value of P_f = 18. The power spectrum $P(\nu,n)$ is smooth until saturation, where trapped-particle instability causes two small sidebands to appear on either side of the fundamental. The evolution of the electron spectrum $f(\nu,n)$ appears tightly bunched up to $n \approx 750$ passes. At $n \approx 750$, sidebands develop which cause the electrons to fill the full height of the separatrix, spreading the electron spectrum.

Figure 18 shows pulse evolution for d = 0.1. The larger desynchronism has advanced the optical pulse so far ahead of the electrons, that the electron pulse is only amplifying the trailing edge of the optical pulse. This leads to a decoupling between the optical pulse and the electrons, which reduces the optical field amplitude to $|a|$ = 5.3.

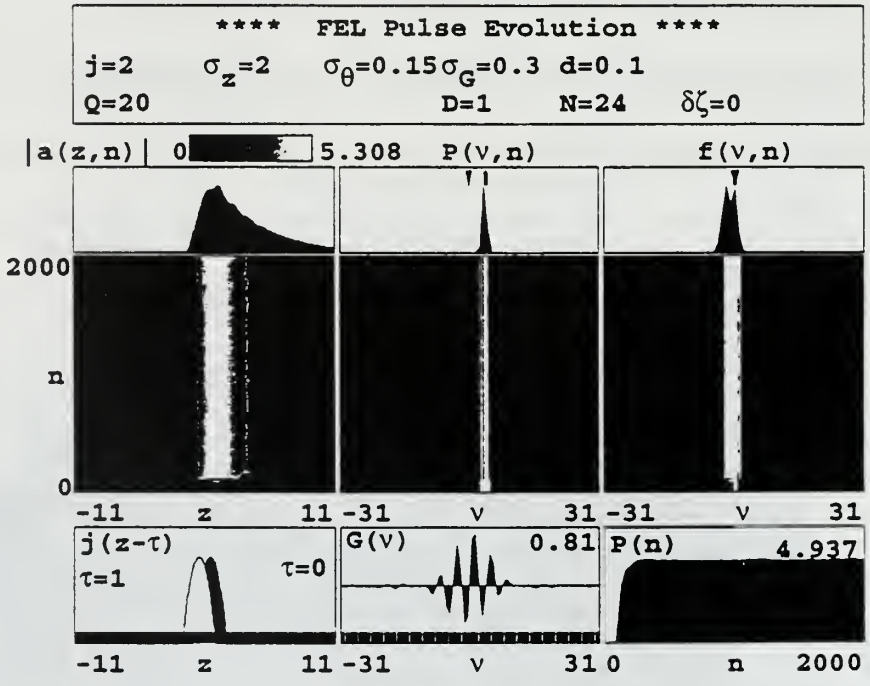

Figure 18. Pulse evolution for D = 1 and d = 0.1.

This optical field amplitude is insufficient for the trapped-particle instability. The resulting power and electron spectrum are narrow, while the final power now only reaches P_f = 5.

Figure 19 shows the pulse evolution for an even larger value of desynchronism, $d = 0.25$. In this case of large d, the optical pulse is artificially advanced well ahead of the electrons, so that the electrons are only amplifying the trailing edge of the optical pulse. This results in weak optical amplitude, so that $|a| = 1$. The power and electron spectrums are narrow for this case and a final power of only $P_f = 1$ is attained.

Figure 20 is a plot of final power versus desynchronism, and is a result of numerous computer simulations with dispersion strengths of $D = 0$ and $D = 1$. The boxes and circles represent computer simulation results, while the line traces the

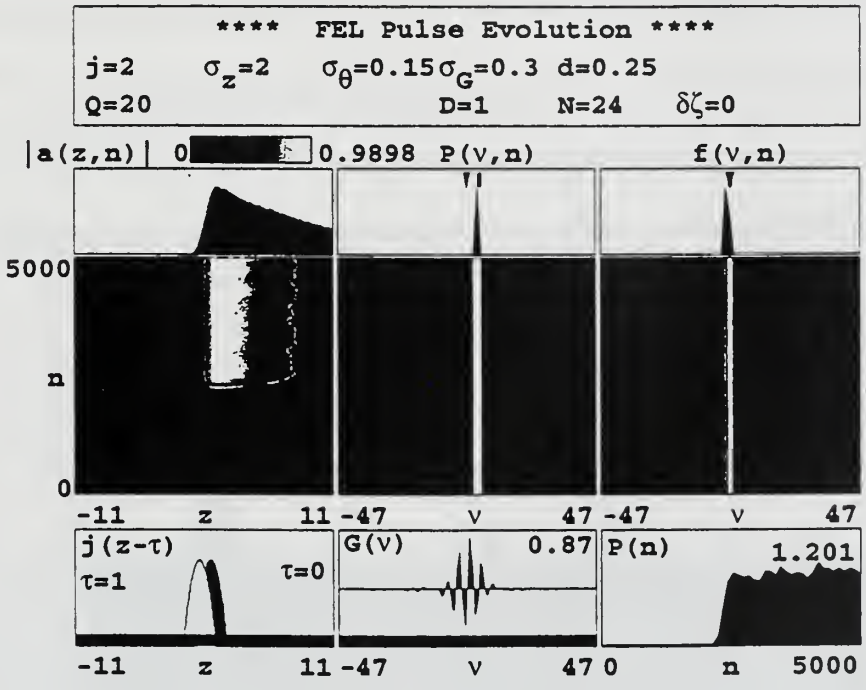

Figure 19. Pulse evolution for $D = 1$ at $d = 0.25$.

curve shape. The maximum final power of $P_f = 94$ occurs at $d = 0.007$ for the conventional undulator ($D = 0$). For larger values of desynchronism, the final power falls off quickly until it reaches zero for $d \approx 0.12$. For a dispersion strength of $D = 1$, the maximum final power $P_f = 7.7$ occurs at $d = 0.003$. The final power decreases until $d =$

0.11 just as in the $D = 0$ case, but then begins a slight increase until $d = 0.20$, where it begins to decrease to zero.

By comparing Figures 18 and 19 and analyzing the pulse evolution simulations between these values of $d = 0.10$ and $d = 0.25$, an explanation is given for this small increase. The final shape of the optical pulse, $|a(z,n)|$, in Figure 18 shows that for $d = 0.10$, the width of the optical pulse is relatively narrow since the leading edge has decreased nearly to zero within the window width. Comparing this optical pulse shape to that in Figure 19 shows that for $d = 0.25$, the leading edge of the optical pulse is much longer, corresponding to a longer pulse width. Analysis of pulse evolution simulations

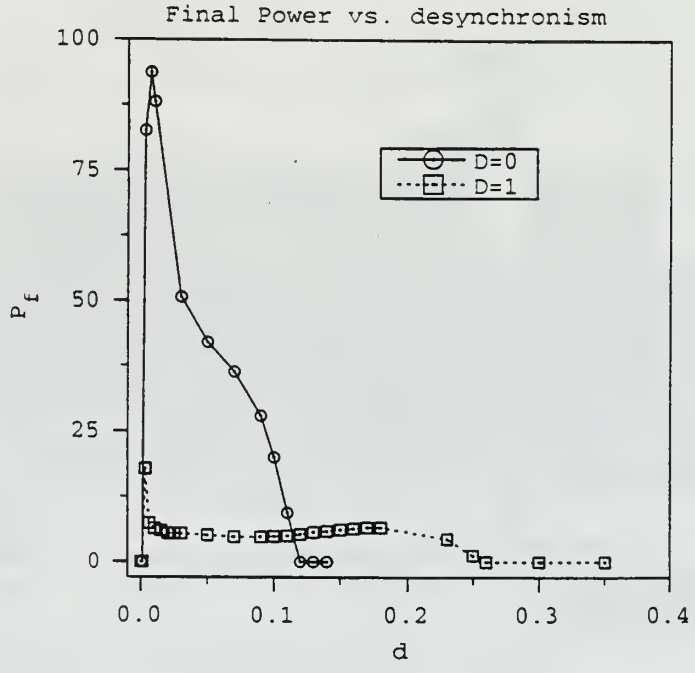

Figure 20. Final power versus desynchronism.

between $d = 0.10$ and $d = 0.20$ show that this leading edge indeed gets longer while the pulse height only slightly decreases. Thus, between $d = 0.10$ and $d = 0.20$, the width of the optical pulse increases at a greater rate than the pulse height decreases, so that there is

a slight increase in the final power. At $d \approx 0.20$, the decreasing rate of the pulse height exceeds the increasing width of the leading edge, so that the final power again decreases to zero. As Figure 20 shows, for larger values of desynchronism, the short pulse effects lead to a decoupling between the optical field and electrons, decreasing the final power until it reaches zero.

B. FINAL GAIN IN WEAK OPTICAL FIELDS

Figure 21 shows the same pulse evolution simulation as Figures 14-19, but now gain as a function of the number of passes, *G(n)*, is shown in the lower-right plot. Electron beam parameters remain unchanged, while the resonator losses, determined by $1/Q = 1/10^{10}$, are extremely small. The desynchronism is $d = 0.04$ in the conventional undulator ($D = 0$). The plot shows $n = 200$ passes in the resonator.

The electron pulse, again approximated with a parabolic shape, appears to be

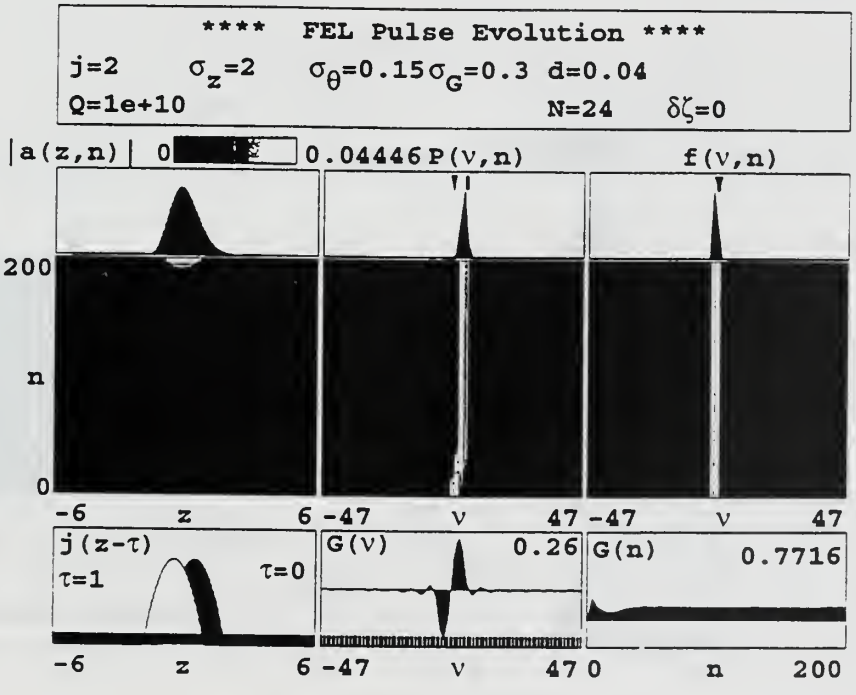

Figure 21. Pulse evolution for weak-field gain with $D = 0$ and $d = 0.04$.

amplifying the entire optical pulse as it travels the undulator. The desynchronism has artificially advanced the optical pulse ahead of the narrow electron pulse, so that the optical field amplitude remains in weak fields with $|a| = 0.045$. In weak fields, the electrons never fully bunch, so that the power spectrum $P(\nu,n)$ and electron spectrum $f(\nu,n)$ remain narrow throughout the n passes. The gain peaks due to transients and the reaches steady state after $n \approx 30$ passes with a final value of $G_f \approx 0.20$. This is the maximum value of final gain for the $D = 0$ case, and plots with varying desynchronism show similar trends with decreased G_f and optical pulses that never fully develop.

Figure 22 shows the FEL evolution for $d = 0.11$ with $D = 1$. The large desynchronism again has artificially advanced the light pulse ahead of the electrons, so that all electrons are not interacting with the optical pulse throughout the undulator. This means that the optical and electron pulse are never fully coupled, which decreases

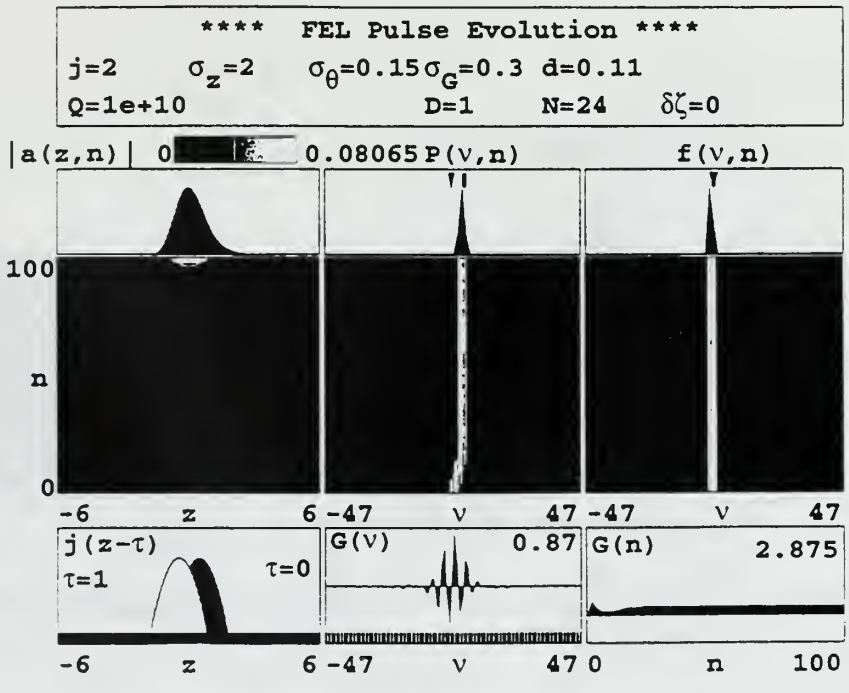

Figure 22. Pulse evolution for weak-field gain with $D = 1$ and $d = 0.11$.

electron bunching and results in an optical field amplitude of $|a| = 0.08$. Again, in the weak-field regime, the power spectrum and electron spectrums are narrow, due to weak fields. The gain appears to peak, again due to transients, and then reaches steady state after $n \approx 30$ passes, reaching a final value of $G_f = 0.16$. For $D = 1$ and varying desynchronism, computer simulations show similar trends with even smaller final gain values.

Figure 23 shows a plot of final gain versus desynchronism in weak optical fields. It combines several computer simulations with dispersion strengths of $D = 0$ and $D = 1$. The boxes and circles represent computer simulation results, while the line traces the curve shape. The maximum gain, $G_f = 0.50$, occurs for $D = 1$ at $d = 0.11$. The final gain quickly drops off for values of desynchronism larger than $d = 0.11$, until it reaches zero at $d \approx 0.26$. For $D = 0$, the conventional undulator, the maximum gain, $G_f = 0.20$, occurs at

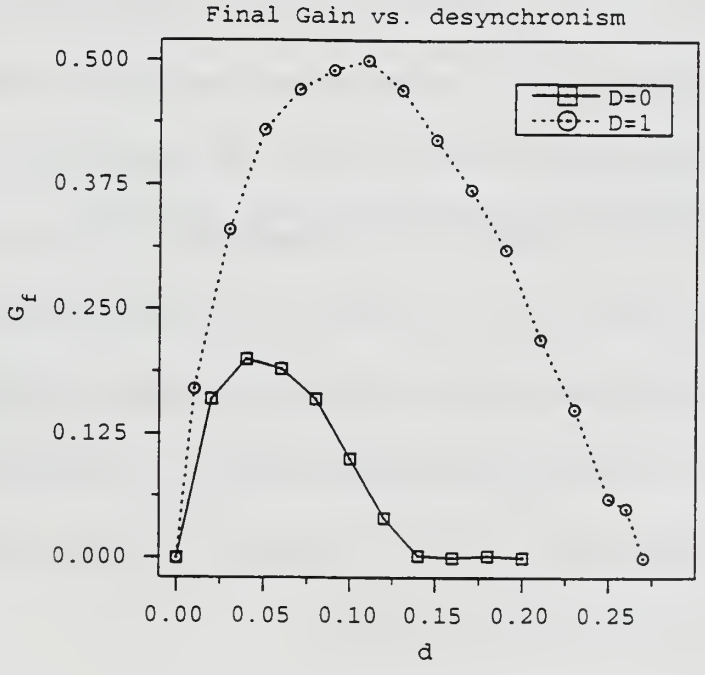

Figure 23. Final gain versus desynchronism.

$d = 0.04$, but this is less than half the maximum final gain of the $D = 1$ case. Again, for larger d values, the final gain decreases until it reaches zero at $d \approx 0.14$.

C. FRACTIONAL SPREAD IN ENERGY

For the TJNAF FEL, an energy spread is critical because the FEL design feeds back electrons through the RF cavities of the accelerator. This feedback loop utilizes steering magnets, which alter the path of electrons and are sensitive to a spread in electron energies. The TJNAF 20 kW FEL design can tolerate an energy spread of 6% induced in the operating FEL [5]. By measuring the full spread in phase velocities, Δv, in the upper-right plot of the pulse evolution simulations, the fractional spread in beam energy, $\Delta\gamma/\gamma$, can be found using the relationship $\Delta v = 4\pi N \Delta\gamma / \gamma$.

Figure 24 shows a plot of the fractional energy spread of the electrons, $\Delta\gamma/\gamma$, versus the desynchronism, d. Simulation results for dispersive strengths of $D = 0$ and $D = 1$ are plotted as boxes and circles, respectively, while the line traces the curve shape. For the conventional undulator, $D = 0$, the energy spread peaks at $\Delta\gamma/\gamma = 8.6\%$, corresponding to a desynchronism value of $d = 0.007$. The energy spread decreases and reaches $\Delta\gamma/\gamma = 6\%$ at $d = 0.03$. After $d = 0.03$, the energy spread continues to decrease until reaching a steady value of $\Delta\gamma/\gamma = 1.7\%$ at $d = 0.12$. The energy spread for all values of $d = 0.03$ and larger remains below the 6% limit specified by TJNAF. For the klystron of strength $D = 1$, the energy spread peaks at $\Delta\gamma/\gamma = 0.05$ corresponding to $d = 0.003$. As Figure 24 shows in the case of $D = 1$, the spread in energies remains below this 5% maximum for all values of desynchronism.

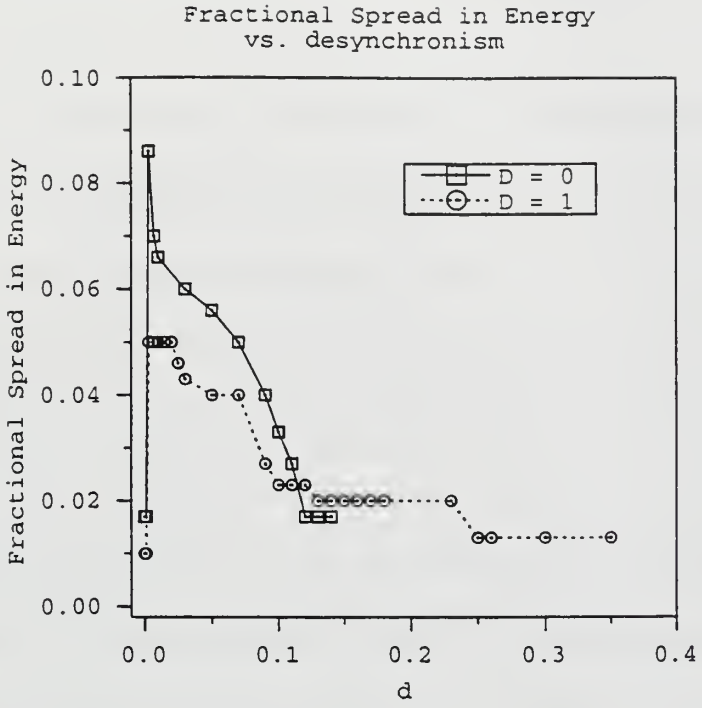

Figure 24. Energy spread versus desynchronism.

V. CONCLUSIONS

With the ever-increasing capability and lethality of anti-ship missiles, and the fixed wavelengths of conventional chemical lasers, U.S. Navy needs a weapon with faster reaction times, longer engagement ranges, and improved accuracy to ensure the safety of surface combatants. The proposed TJNAF 20 kW FEL offers potential in fulfilling these capability requirements well into the future.

Simulations showed that the peak final power occurred at smaller values of desynchronism. For the case of a conventional undulator, $D = 0$, the maximum final power, $P_f = 94$, occurring at a desynchronism value of $d = 0.007$. For a klystron undulator with a dispersion strength of $D = 1$, the peak final power, $P_f = 18$ occurring at $d = 0.003$. Figure 20 showed that there was a slight increase in the final power between $d = 0.11$ and $d = 0.20$, and for larger desynchronism the final power decreased.

Figure 25 shows the final power of the TJNAF FEL in kilowatts versus desynchronism, d. When the conversion is done, the dimensionless power, $P_f = 94$, corresponds to a power of 36 kW, exceeding TJNAF's goal of only 20 kW. For the maximum power of the $D = 1$ case, the final power is only $P = 7$ kW, which is a significant amount of power but well below the anticipated 20 kW.

Simulations with the weak-field gain showed that the maximum gain, $G_f = 50\%$, occurring in the klystron of strength $D = 1$ for a relatively large desynchronism value of $d = 0.11$. For the case of a conventional undulator, $D = 0$, the maximum gain found is $G_f = 20\%$, occurring at a smaller desynchronism value of $d = 0.04$. At larger desynchronism, the gain decreases steadily to zero.

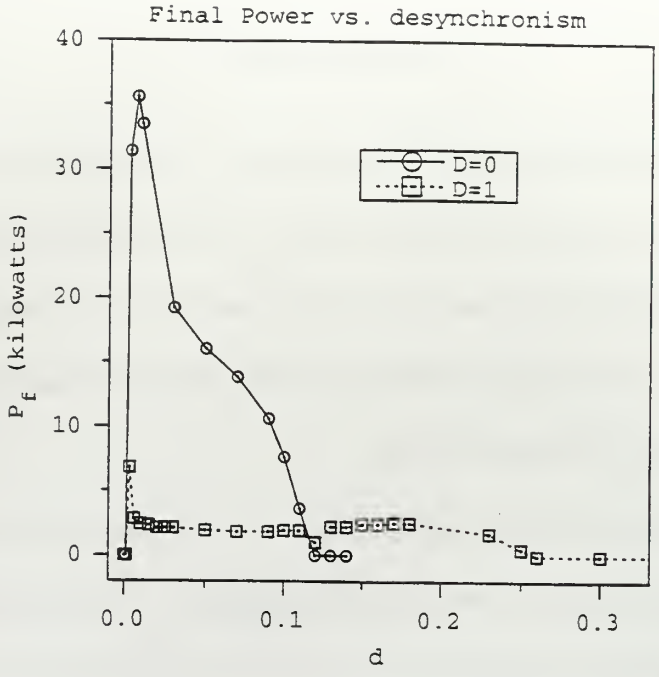

Figure 25. Final power in kilowatts versus desynchronism.

In order ensure feedback of recirculating electrons back to the RF cavities of the accelerator, the induced electron energy spread was measured and compared to TJNAF's goal of 6% or less. Figure 24 shows that the maximum energy spread, $\Delta\gamma/\gamma = 0.086$, occurs for the conventional undulator with $D = 0$ at $d = 0.007$. The induced energy spread decreases and reaches 6% at values of $d = 0.03$ and larger. For a dispersion strength of $D = 1$, the energy spread peaks at $\Delta\gamma/\gamma = 5\%$ corresponding to $d = 0.003$, which is below the 6% goal. In fact, for the $D = 1$ case, the energy spread is less than 6% for all d values.

Based on the above simulation results and the information contained in Figures 20, 23 and 24, the optimum value of desynchronism is $d = 0.03$ using a conventional undulator with $D = 0$. At this value, the energy spread is 6%, which achieves TJNAF's design goal to ensure proper electron feedback. The final power corresponding to $d = 0.03$ and $D = 0$ is $P = 19.2$ kW, which is close to the 20 kW objective and corresponds to

a final gain of $G_f = 19\%$.

These simulations combined various values of desynchronism and undulator dispersive strengths in order to evaluate the effects on final power and final gain at the output of the resonator, and electron beam energy spread with regard to the feedback loop. With continued improvements in the design based on these simulations and further thesis work, the proposed TJNAF 20 kW FEL could significantly advance the technology needed to defend Navy combatants against anti-ship missile threats in the future.

LIST OF REFERENCES

[1] J. Albertine and J.R. Cook,"High Energy Laser Weapon System", *Surface Warfare*, September/October 1997, Vol. 22, No. 5.

[2] J. Albertine and J.R. Cook,"High Energy Laser Weapon System", *Surface Warfare*, September/October 1997, Vol. 22, No. 5.

[3] E. J. Anderson, "Total Ship Integration of a Free Electron Laser (FEL)," Master's Thesis, Naval Postgraduate School, September 1996.

[4] W.B. Colson, "Classical Free Electron Laser Theory," *Free Electron Laser Handbook*, W.B. Colson, C. Pellegrini, and A. Renieri (eds.), North-Holland Physics, Elsevier Science Publishing Co. Inc., The Netherlands, 1990.

[5] S. Benson, personal communication.

INITIAL DISTRIBUTION LIST

1. Defense Technical Information Center 2
   8725 John J. Kingman Rd., STE 0944
   Ft. Belvoir, Virginia 22060-6218

2. Dudley Knox Library 2
   Naval Postgraduate School
   441 Dyer Rd.
   Monterey, CA 93943-5101

3. Professor William B. Colson, Code PH/Cw 4
   Department of Physics
   Naval Postgraduate School
   Monterey, CA 93943-5117

4. Professor Robert L. Armstead, Code PH/Ar 1
   Department of Physics
   Naval Postgraduate School
   Monterey, CA 93943-5117

5. Lieutenant Richard B. Steele, USN 2
   14061 Cork St.
   Garden Grove, CA 92644

6. John Albertine 1
   109 Kingswood Rd.
   Annapolis, MD 21401

7. Joung R. Cook 1
   Research Physicist, Code 6655
   Naval Research Laboratory
   4555 Overlook Drive, SE
   Washington, DC 20375-5000

8. Fred Dylla 1
   TJNAF
   12000 Jefferson Avenue
   Newport News, VA 23606

9. George Neil 1
TJNAF
12000 Jefferson Avenue
Newport News, VA 23606